Environmental Effects on Aerosol-Cloud Interaction in non-precipitating MBL Clouds over the Eastern North Atlantic

Xiaojian Zheng[1], Baike Xi[1], Xiquan Dong[1], Peng Wu[2], Yuan Wang[3,4] and Timothy Logan[5]

[1]Department of Hydrology and Atmospheric Sciences, University of Arizona, Tucson, AZ, USA

[2]Pacific Northwest National Laboratory, Richland, WA, USA

[3]Division of Geological and Planetary Sciences, California Institute of Technology, Pasadena, CA, USA

[4]Jet Propulsion Laboratory, California Institute of Technology, Pasadena, CA, USA

[5]Department of Atmospheric Sciences, Texas A&M University, College Station, TX, USA

Correspondence: Baike Xi (baikex@arizona.edu)

Abstract. Over the eastern north Atlantic (ENA) ocean, a total of 20 non-precipitating single-layer marine boundary layer (MBL) stratus and stratocumulus cloud cases are selected to investigate the impacts of the environmental variables on the aerosol-cloud interaction (ACI_r) using the ground-based measurements from the Department of Energy Atmospheric Radiation Measurement (ARM) facility at the ENA site during 2016 – 2018. The ACI_r represents the relative change of cloud-droplet effective radius r_e with respect to the relative change of cloud condensation nuclei (CCN) number concentration at 0.2% supersaturation ($N_{CCN,0.2\%}$) in the water vapor stratified environment. The ACI_r values vary from -0.01 to 0.22 with increasing sub-cloud boundary layer precipitable water vapor (PWV_{BL}) conditions, indicating that r_e is more sensitive to the CCN loading under sufficient water vapor supply, owing to the combined effect of enhanced condensational growth and coalescence processes associated with higher N_c and PWV_{BL}. The principal component analysis shows that the most pronounced pattern during the selected cases is the co-variations of the MBL conditions characterized by the vertical component of turbulence kinetic energy (TKE_w), decoupling index (D_i) and PWV_{BL}. The environmental effects on ACI_r emerge after the data are stratified into different TKE_w regimes. The ACI_r values, under both relatively lower and higher PWV_{BL} conditions, increase more than double from the low TKE_w to high TKE_w regime. It can be explained by the fact that stronger boundary layer turbulence maintains a well-mixed MBL, strengthening the connection between cloud microphysical properties and underneath CCN and moisture sources. With sufficient water vapor and low CCN loading, the active coalescence process

broadens the cloud droplet size spectra, and consequently results in an enlargement of r_e. The enhanced N_c conversion and condensational growth induced by more intrusions of CCN effectively decrease r_e, which jointly presents as the increased ACI_r. This study examines the importance of environmental effects on the ACI_r assessments and provides observational constraints to future model evaluations on aerosol-cloud interactions.

1. Introduction

Clouds are one of the most important parts of the Earth's climate system. They can impact the global climate by modulating the radiative balance in the atmosphere. Moreover, the radiative effects of cloud adjustments due to aerosols remain one of the largest uncertainties in climate modeling (IPCC, 2013). Over the oceanic area, the lower troposphere is dominated by marine boundary layer (MBL) clouds. MBL clouds can persistently reflect the solar radiation by their long-lasting nature maintained by cloud-top radiative cooling, and therefore act as a major modulator of the Earth radiative budget (Seinfeld et al., 2016). The climatic importance of MBL cloud radiative properties is primarily induced by cloud microphysical properties, namely the cloud-droplet number concentration (N_C), and effective radius (r_e), and has been intensively investigated by many researchers (Garrett and Zhao, 2006; Rosenfeld, 2007; Wood et al., 2015; Seinfeld et al., 2016). The ambient aerosol conditions can influence these cloud microphysical properties via the aerosol-cloud interaction (ACI). Compared to the clean regions, clouds under the regions having relatively higher below-cloud aerosol concentrations exhibited more small cloud droplets (reduced r_e and increased N_C) and enhanced both cloud liquid water contents and optical depths (McComiskey et al., 2009; Chen et al., 2014; Wang et al., 2018). The changes of MBL cloud microphysical properties induced by aerosols have been investigated from previous studies using in-situ measurements, ground- and satellite-based observations, and model simulations in multiple oceanic areas such as the eastern Pacific and eastern Atlantic (Twohy et al., 2005; Lu et al., 2007; Hill et al., 2009; Costantino and Bréon, 2010; Mann et al., 2014; Dong et al., 2015; Diamond et al., 2018; Yang et al., 2019; Zhao et al., 2019; Wang et al., 2020).

The assessments of ACI, particularly using ground-based remote sensing, vary in terms of the quantitative values, which represent the different cloud susceptibilities to aerosol loadings. Owing to the numerous approaches in assessing the ACI, such as the spatial and temporal scales, N_c and r_e retrieval methods, and more importantly, the different aerosol proxies used in the ACI quantification, different ACI results could be achieved. For example, the studies using total aerosol number concentration and

aerosol scattering/extinction coefficients to represent the aerosol loadings would result in relatively lower ACI values (Pandithurai et al., 2009; Liu et al., 2016). This is primarily attributed to the inclusion of aerosol species with different abilities to activate, which is determined by their physicochemical properties, and thus will cause non-negligible uncertainties in capturing the information of aerosol intrusion to the cloud (Feingold et al. 2006; Logan et al., 2014). While some studies found relatively higher ACI values using cloud condensation nuclei (CCN) number concentration (N_{CCN}), presumably due to the fact that CCN represents the portion of aerosols that can be activated and possesses the potential ability to further grow into cloud droplets, this favorably yields a more straightforward assessment of ACI (McComiskey et al., 2009; Qiu et al., 2017; Zheng et al., 2020). It is noteworthy that the ACI variations have been found to have both increasing and decreasing trends in response to changing environmental water availability (Martin et al., 2004; Kim et al., 2008; McComiskey et al., 2009; Pandithurai et al., 2009; Martin et al., 2011; Liu et al., 2016; Zheng et al., 2020). Although these contradicting results have been postulated due to multiple factors such as cloud adiabaticity, condensational growth, collision coalescence, and atmospheric thermodynamics and dynamics, the underlying mechanisms in altering the ACI and causing the uncertainties in the ACI assessments remain unclear. Therefore, further studies are necessary (Fan et al., 2016; Feingold and McComiskey, 2016; Seinfeld et al., 2016).

The Eastern North Atlantic (ENA) is a remote oceanic region that features persistent but diverse subtropical MBL clouds, owing to complex meteorological influences from the semi-permanent Azores High and prevailing large-scale subsidence (Wood et al., 2015). The ENA has become a favorable region to study the aerosol indirect effects on MBL clouds under a relatively clean environment with occasional intrusions of long-range transport of continental air mass (Logan et al., 2014; Wang et al., 2020). The atmospheric radiation measurement (ARM) program established the ENA permanent observatory site on the northern edge of Graciosa Island, Azores, in 2013, which continuously provides comprehensive measurements of the atmosphere, radiation, cloud, and aerosol from ground-based observation instruments. Owing to the location of the site, where sits in between the boundaries of mid-latitude and subtropical regimes, the ENA is under the mixed influence of diverse meteorological conditions. So that in terms of the aerosol influence on the cloud properties, the roles of meteorological factors on cloud formation and development are not negligible and hence are being explored in this study. The large-scale thermodynamic variables of the lower troposphere are widely used, such as the lower tropospheric stability (LTS), where the higher LTS values are found to be associated with a relatively shallow and well-mixed marine boundary layer, and are prone to stratiform cloud formations with higher cloud fractions (Klein and Hartmann, 1993; Wood, 2012; Wood and Bretherton, 2006; Yue et al., 2011;

Rosenfeld et al., 2019), especially over the subtropical ocean such as the southeast Atlantic. Over the ENA site, the spatial gradient of the LTS has been studied to be associated with the contribution terms of MBL turbulence and the wind directional change (Wu et al., 2017).

In the cloud-topped MBL which is maintained by cloud-top radiative cooling, the buoyancy generations and shears contribute most to the turbulence kinetic energy (TKE) production (Nicholls, 1984; Hogan et al., 2009), where the intensity of turbulence denotes the coupling of MBL clouds to the below-cloud boundary layer. In terms of the cloud droplet growing process, especially in a clean environment with low N_{CCN} below the cloud layer, the cloud droplets at the cloud base experience rapid growth via the diffusion of water vapor, and subsequently enter the regime of active coalescence (Rosenfeld and Woodley, 2003; Martins et al., 2011). The intensive turbulence effectively modulates the cloud droplet growth by strengthening the coalescence process and the cloud cycling (Feingold et al., 1996, 1999; Pawlowska et al., 2006). And particularly giving the unique topography of the Graciosa Island, the island effect would cause disturbances on the updraft and hence impact the MBL turbulence, depending on the surface wind directions (Zheng et al., 2016). The environmental effects on the MBL cloud formation and development processes and cloud microphysical properties have been widely implemented and considered in climate modeling (Medeiros and Stevens, 2011; West et al., 2014; Zhang et al., 2016). Thus, it is important to provide observational constraints on the environmental effects. The assessment of ACI from the ground-based perspective highly relies on the sensitivities of cloud droplet number concentrations and size distribution to the changing of below-cloud CCN loadings. Hence, studying the relationship between the environmental effect and the MBL cloud microphysical responses is a nontrivial task.

In this study, we target the non-precipitating single-layer MBL stratus and stratocumulus clouds during the period between September 2016 and May 2018 and examine the role of thermodynamical and dynamical variables on ACIs. This study aims to advance the understanding of ACI by disentangling the environmental effects and providing observational constraints on quantifying the ACI when modeling aerosol effects on MBL clouds. The ground-based observations and retrievals, and the reanalysis are introduced in section 2. Section 3 describes the aerosol, cloud and meteorological properties, and the variations of cloud microphysical properties under different environmental regimes. Moreover, the ACIs under given water vapor conditions and the roles of environmental effects on ACI are discussed in Section 3. The conclusion of the key findings and the future work are presented in section 4.

2. Data and methods

2.1 Cloud and aerosol properties

131   The cloud boundaries at the ARM ENA site are primarily determined by the ARM Active Remotely-
132   Sensed Cloud Locations (ARSCL) product, which is a combination of data detected by multiple active
133   remote-sensing instruments, including the Ka-band ARM Zenith Radar (KAZR) and laser ceilometer.
134   The KAZR has an operating frequency at 35 GHz and is sensitive in cloud detection with very minimum
135   attenuation up to the cloud top height (Widener et al., 2012). The temporal and vertical resolutions of
136   KAZR reflectivity are 4 seconds and 30 m, respectively. The ceilometer operates at 910 nm and its
137   attenuated backscatter data can be converted to the cloud base height up to 7.7 km with an uncertainty
138   of ~10 m (Morris, 2016). Combing both KAZR and ceilometer measurements, the cloud base (z_b) and
139   top (z_t) heights can be identified accordingly. The single-layer low cloud is defined as having a cloud
140   top height lower than 3 km, with no additional cloud layer in the atmosphere above (Xi et al., 2010).

141   The cloud microphysical properties are retrieved from a combination of ground-based observations,
142   including KAZR, ceilometer, and microwave radiometer. The detailed retrieval methods and procedures
143   are described in Wu et al. (2020a). The retrieved cloud microphysical properties, both in time series and
144   vertical profiles, have been validated using the collocated aircraft in-situ measurements during the
145   Aerosol and Cloud Experiments in the Eastern North Atlantic field campaign (ACE-ENA). The retrieval
146   uncertainties are estimated to be ~15% for cloud droplet effective radius (r_e), ~35% for cloud droplet
147   number concentration (N_c), and ~30% for the cloud liquid water content (LWC) (Wu et al., 2020a).
148   Furthermore, the cloud adiabaticity is calculated using the retrieved in-cloud vertical profile of LWC and
149   the adiabatic LWC_{ad}. The LWC_{ad} is given by $LWC_{ad(z)} = \Gamma_{ad}(z - z_b)$, following the method in Wu et
150   al. (2020b), where Γ_{ad} denotes the linear increase of LWC with height under an ideal adiabatic condition
151   (Wood, 2005). The cloud adiabaticity (f_{ad}) is defined as the ratio of LWC to LWC_{ad}.

152   The surface CCN number concentrations (N_{CCN}) are measured by the CCN-100 (single-column)
153   counter. Since the supersaturation (SS) levels are set to cycling between 0.10% and 1.10% approximately
154   within one hour, N_{CCN} under a relatively stable supersaturation level has to be carefully calculated to rule
155   out the impact of supersaturation on N_{CCN}. This study adopts the interpolation method given by $N_{CCN} = cSS^k$ (Twomey, 1959), where parameters c and k are fitted by a power-law function for every periodic
157   cycle. In this study, the supersaturation level of 0.2% is used because it represents typical supersaturation
158   conditions of boundary-layer stratiform clouds (Hudson and Noble, 2013; Logan et al., 2014; Wood et
159   al., 2015; Siebert et al., 2021), and N_{CCN} at 0.2% supersaturation (hereafter $N_{CCN,0.2\%}$) is interpolated to
160   5-min temporal resolution.

161

162   **2.2 Environmental conditions and cloud case selections**

The integrated precipitable water vapor (PWV) is obtained from a 3-channel microwave radiometer (MWR3C), which operates at three frequency channels of 23.834, 30, and 89 GHz. The uncertainty of PWV is estimated to be ~0.03 cm (Cadeddu et al., 2013). To capture the information of MBL water vapor more accurately, the sub-cloud boundary layer integrated precipitable water vapor (PWV_{BL}) is calculated using the interpolated sounding product following:

$$PWV_{BL} = \frac{1}{\rho_w} \sum (z_{i+1} - z_i) * (\rho_{v,i+1} + \rho_{v,i})/2, \tag{1}$$

where the ρ_w is the liquid water density and the ρ_v is the water vapor density collected from the Interpolated Sounding and Gridded Sounding Value-Added Products (Toto and Jensen, 2016), the subscripts i and $i+1$ represent the bottom and top of each interpolated sounding height layer. Both PWV and PWV_{BL} are temporally collocated to 5-min resolution and plotted against each other in Fig. S1a to test the contribution of PWV_{BL} to the PWV. The Pearson correlation coefficient of 0.85 shows that the PWV_{BL} are strongly positively correlated with the PWV, while the distribution of the percentage ratio of PWV_{BL} to PWV (Fig. S1b) indicates that, on average, the PWV_{BL} contribute to ~58% of the PWV. Considering the cloud-topped MBL, the majority of cases (~74%) associate with a relatively moist boundary layer compared to the amount of water vapor in the free troposphere, where the PWV_{BL} already contributed over 50% of the total column PWV. In contrast, only ~9% of cloud samples occur under a relatively dry boundary layer and moist free troposphere, where PWV_{BL} contributions are less than 40%. In general, the PWV can well capture the variation of the PWV_{BL}. In the rest of the study, the PWV_{BL} are used, as it represents the sub-cloud boundary layer water vapor availabilities which are more closely related to the MBL cloud processes.

The LTS parameter is used as a proxy of large-scale thermodynamic structure and is defined as the difference between the potential temperature at 700 hPa and surface ($\theta_{700} - \theta_{sfc}$). The LTS values are calculated from European Centre for Medium-Range Weather Forecasts (ECMWF) model outputs of potential temperature, by averaging over a grid box of 0.56°×0.56° centered at the ENA site. To match the temporal resolutions of the other variables, the original 1-hour LTS data are downscaled to 5-min under the assumption that the large-scale forcing would not have significant changes within an hour.

The boundary layer decoupling condition is represented by the decoupling index (D_i), which is given by $D_i = (z_b - z_{LCL})/z_b$, where the z_{LCL} is the lifting condensation level calculated analytically following the method in Romp (2017), with an uncertainty of around 5 m. The surface temperature, pressure, relative humidity, and mass fraction of water vapor that used in the z_{LCL} calculation, as long as

193   the vector-averaged wind directions (in 360° coordinate) over the ENA site are obtained from the ARM

194   surface meteorology systems (ARM MET handbook, 2011).

195   As for the boundary layer dynamics, the higher-order moments of vertical velocity are widely used

196   in different model parameterization practices, such as higher-order turbulence closure and probability

197   density function methods (Lappen and Randall, 2001; Zhu and Zuidema, 2009; Ghate et al., 2010). The

198   vertical velocity variance can be used to represent the turbulence intensity in the below-cloud boundary

199   layer (Feingold et al., 1999). In this study, the vertical component of the turbulence kinetic energy (TKE_w)

200   are used, which is defined as:

201    $TKE_w = \frac{1}{2}\overline{(w')^2}$,   (2)

202   where the $(w')^2$ is the variance of vertical velocity measured from the Doppler lidar standard 10-min

203   integration, which is collected in the Doppler Lidar Vertical Velocity Statistics Value-Added Product

204   (Newson et al., 2019). The noise correction has been applied to reduce the uncertainty of the variance to

205   ~10% (Hogan et al., 2009; Pearson et al., 2009). In this study, the mean value of TKE_w in the sub-cloud

206   boundary layer proportion of the Doppler lidar range is used, and the data temporal resolution is further

207   downscaled to 5-min for temporal collocation purposes.

208   In this study, the non-precipitating cloud periods are determined when the KAZR reflectivity at the

209   ceilometer-detected cloud base height range does not exceed -37 dBZ (Wu et al., 2015, 2020b), which

210   extensively rules out the wet-scavenging depletion on below-cloud CCN (Wood, 2006) and ensures the

211   accuracy in capturing the below-cloud CCN loadings. Both retrieved cloud microphysical properties and

212   CCN data are available from September 2016 to May 2018 and confine this period in this study.

213

214   **3. Result and Discussion**

215   **3.1 Aerosol, cloud, and meteorological properties of selected cloud cases**

216   A total of 20 non-precipitating cloud cases are selected in this study, with the detailed time periods

217   listed in Table 1, including 1143 samples with temporal resolution of 5-min, which corresponds to ~95

218   hours. Among the selected cases, there are three, eight, five, and four cases for Spring, Summer, Fall,

219   and Winter seasons, respectively. MBL clouds often produce precipitation in the form of drizzle (Wood

220   2012, Wu et al., 2015, 2020b). A recent study of the seasonal variation of the drizzling frequencies (Wu

221   et al., 2020b) showed that the MBL clouds in the cold months (Oct-Mar) have the highest drizzling

222   frequency of the year (~70%), while the clouds in the warm months (Apr-Sept) are found to have a lower

223   chance of drizzling (~45%). Therefore, the selection of a non-precipitating single-layer low cloud case

224   that lasts at least 2 hours is limited, with only 6 cases found in the cold months and 14 cases found during
225   the warm months.

226   The probability distribution functions (PDFs) of the aerosol and cloud properties, and the
227   environmental conditions for the selected cases are shown in Fig. 1. The PDF of $N_{CCN,0.2\%}$ presents a
228   normal distribution with a mean value of 215 cm^{-3} and median value of 217 cm^{-3}. About 97% of the
229    $N_{CCN,0.2\%}$ samples lie below 350 cm^{-3} and represents a relatively clean environment (Logan et al., 2014,
230   2018). A few instances of aerosol intrusions (~3%) with higher $N_{CCN,0.2\%}$ were likely a result of
231   continental air mass transport from North America, Europe, and Africa (Logan et al., 2014; Wang et al.,
232   2020). As for the cloud microphysical properties, the cloud-layer mean N_c and r_e (Fig. 1b and 1c) are
233   also both normally distributed with median values close to the mean values. The majority of the N_c
234   values (~91%) are lower than 125 cm^{-3} with a mean value of 86 cm^{-3}, and the r_e distribution peaks at
235   9 - 11 μm with a mean value of 10.1 μm. Both N_c and r_e values fall in the typical ranges of the non-
236   precipitating MBL cloud characteristics over the ENA site (Dong et al., 2014; Wu et al., 2020b). The
237   distribution of f_{ad} is slightly skewed to the left with a median value of 0.66 (Fig. 1d), indicates that the
238   bulk of cloud samples are close to adiabatic environments, while the left tail denotes a wide range of
239   cloud sub-adiabaticities, which allows us to investigate the role of cloud adiabaticities on the cloud
240   microphysical variations.

241   For all selected cases, the LTS, which represents the large-scale thermodynamic structure, is
242   distributed bimodally across the range from 14K to 23K with mean and median values of 19.1K in Fig.
243   1e. A higher LTS magnitude represents a relatively stable environment and is favorable to the formation
244   of marine stratocumulus (Medeiros and Stevens, 2011; Gryspeerdt et al., 2016). Note that the median
245   LTS of 19.1 K in this study is close to the separation threshold of 18.55K suggested by prior studies to
246   distinguish the marine stratocumulus from a global assessment of marine shallow cumulus clouds
247   (Smalley and Rapp, 2020). Therefore, leveraging the demarcation line at 19.1K may allow us to
248   investigate the aerosol-cloud relationships under contrasting thermodynamic regimes. The PDF of D_i
249   parameter spreads widely with a median value of 0.34 for the selected cases (Fig. 1f), which provides an
250   opportunity to study the cloud sample behaviors under MBL conditions range from well-mixed to
251   decoupled. Higher D_i values indicate more decoupled MBL with weaker turbulence which cannot
252   sufficiently maintain the well-mixed MBL, while lower D_i values often associate with stronger
253   turbulence which maintains a coupled MBL (Jones et al., 2011). As an indicator of the below-cloud
254   boundary layer turbulence, the TKE_w values present a gamma distribution that is highly skewed to the
255   right (Fig. 1e), with a mean value of 0.11 and a median value of 0.08 m^{2}s^{-2}. About half of the cloud

256   samples are under relatively less turbulent environment (which is also implied by the higher half of D_i),
257   suggesting weak connections between the cloud layer and the below-cloud boundary layer. The other
258   half of the cloud samples, with relatively higher TKE_w values up to 0.4 m^2/s^2, imply tighter connections
259   between cloud microphysical properties and below-cloud boundary layer accompanied by intensive
260   turbulent conditions, which is favorable to enhance cloud droplet growth (Albrecht et al., 1995; Hogan
261   et al., 2009; Ghate et al., 2010; West et al., 2014; Ghate and Cadeddu, 2019).

262   It is noteworthy that PWV_{BL} values exhibit a bimodal distribution with a median value of 1.2 cm
263   (Fig. 1f). About 49% of the samples have their PWV_{BL} values in the range of 0.4 - 1.2 cm with the first
264   peak in 0.6 - 0.8 cm, and 51% of the samples have PWV_{BL} values higher than 1.2 cm with a second peak
265   in 1.6 - 1.8 cm, which may be due to the seasonal difference of the selected cases. Fig. S2 shows the
266   seasonal variation of the PWV_{BL} from 2016 to 2018 when single-layered low clouds are present. The
267   monthly PWV_{BL} values are as low as ~ 0.9 cm and remain nearly invariant from January through March,
268   then increase to ~ 2.0 cm (doubled) in September, and decrease dramatically to the winter months. The
269   selected cloud cases are distributed across the seasons, with ~34% of the samples occurring during the
270   months with the lowest mean PWV_{BL} (Jan-Mar), while ~43% of the samples fall in the highest PWV_{BL}
271   months (Jun-Sept). These two different PWV_{BL} regions will provide a great opportunity for us to further
272   examine the ACI under relatively lower and higher water vapor conditions.

273

274   **3.2 Dependent of cloud microphysical properties on CCN and PWV_{BL}**

275   Figure 2 shows the cloud microphysical properties as a function of $N_{CCN,0.2\%}$ and PWV_{BL} for the
276   samples from 20 selected cases. As illustrated in Fig. 2a, there is a statistically significant positive
277   correlation (R^2=0.9) between $ln(N_c)$ and $\ln(N_{CCN,0.2\%})$. The linear fit of $ln(N_c)$ to $\ln(N_{CCN,0.2\%})$ is then
278   mathematically transformed to a power-law fitting function of N_c to $N_{CCN,0.2\%}$, and plotted as dash lines
279   in Fig. 2a. The power-law fitting indicates that 90.3% of the variation in binned $ln(N_c)$ can be explained
280   by the change in the binned $ln(N_{CCN,0.2\%})$ and further suggests that with more available below-cloud
281   CCN, higher number concentrations are expected. The logarithmic ratio $\partial ln(N_c)/\partial ln(N_{CCN,0.2\%})$ is
282   computed to be 0.435 from our study. This ratio is very close to 0.48 found by McComiskey et al. (2009),
283   who also used ground-based measurements to study the marine stratus clouds over the California coast.
284   The logarithmic ratio (0.435) is also close to the result (0.458) of Lu et al. (2007) who used aircraft in-
285   situ measured cloud droplet and accumulation mode aerosol number concentration for the marine stratus
286   and stratocumulus clouds over the eastern Pacific Ocean. The ratio reflects the relative conversion
287   efficiency of cloud droplets from the CCN, regardless of the water vapor availabilities. Theoretically, it

288   has the boundaries of 0 - 1, where the lower bound means no change of N_c with N_{CCN}, and the upper

289   bound indicates a linear relationship that every CCN would result in one cloud droplet. Our result is

290   comparable with the previous studies targeting the MBL stratiform clouds, indicating a certain similarity

291   of the bulk cloud microphysical responses with respect to aerosol intrusion in those types of cloud and

292   over different marine environments, further support that the assessment in this study is valid.

293   The PWV$_{BL}$ values are represented as blue circles (larger one for higher PWV$_{BL}$) in Fig. 2a in order

294   to study the role of water vapor availability on the CCN-N_c conversion process. As demonstrated in Fig.

295   2a, the PWV$_{BL}$ values almost mimic the increasing $N_{CCN,0.2\%}$ trend, which is also governed by the

296   seasonal $N_{CCN,0.2\%}$ and the selected cloud cases. Fig. S3 shows the seasonal variation of $N_{CCN,0.2\%}$ from

297   2016 to 2018. It is noticeable that the monthly $N_{CCN,0.2\%}$ values, which mimic the monthly variation of

298   PWV$_{BL}$, are much higher during warm months (May-Oct) than during cold months (Nov-Apr). This

299   seasonal $N_{CCN,0.2\%}$ variation is also found in recent studies of MBL aerosol composition and number

300   concentration. During the warm months, the below-cloud boundary layer is enriched by the accumulation

301   mode of sulfate and organic particles via local generation and long-range transport induced by the semi-

302   permanent Azores High, which are found to be hydrophilic and can be great CCN contributors (Wang et

303   al., 2020; Zawadowicz et al., 2020; Zheng et al., 2018, 2020). Therefore, the coincidence of high

304   $N_{CCN,0.2\%}$ and PWV$_{BL}$ does not necessarily imply a physical relationship, but instead is the result of their

305   similar seasonal trend. The potential co-variabilities between $N_{CCN,0.2\%}$ and PWV$_{BL}$, and hence the

306   implication on the N_c variation will be further investigated in the latter section. When taking the PWV$_{BL}$

307   into account, R^2 increases from 0.903 to 0.982, and this new relationship suggests that the co-variability

308   between the binned $ln(N_{CCN,0.2\%})$ and ln (PWV$_{BL}$) are in a stronger correlation with the change in

309   binned $ln(N_c)$. Intuitively, if the CCN-N_c relationship is primarily dominated by the diffusion of water

310   vapor, more CCN and higher PWV$_{BL}$ should result in a continuously increasing of N_c. However, the

311   rapid increase of N_c (37 to 92 cm^{-3}) in the first half of $N_{CCN,0.2\%}$ bins (<250 cm^{-3}) does not happen in

312   the second half of the $N_{CCN,0.2\%}$ bins (>250 cm^{-3}) where the slope of N_c increase (96 to 103 cm^{-3})

313   appears to be flattened for higher $N_{CCN,0.2\%}$ and PWV$_{BL}$ bins. Furthermore, the joint power-law fitting of

314   N_c (to $N_{CCN,0.2\%}$ and PWV$_{BL}$) appears to be constantly lower than the single power-law fitting of N_c (to

315   $N_{CCN,0.2\%}$ solely) in each bin. The negative power of PWV$_{BL}$ in this relationship suggests that PWV$_{BL}$

316   might play a stabilization role in the diffusional growth process, which will be further analyzed in the

317   following sections.

318   The relationship between r_e and $N_{CCN,0.2\%}$ is shown in Fig. 2b where there is no significant

319   relationship between r_e with $N_{CCN,0.2\%}$ solely, given a near-zero slope and the low correlation coefficient

320   (fitted line not plotted). However, after applying a multiple linear regression to the logarithmic form of

321   r_e, $N_{CCN,0.2\%}$ and PWV_{BL}, a significant correlation among those three variables is found. The r_e is

322   negatively correlated with $N_{CCN,0.2\%}$ and positively correlated with PWV_{BL}, and 73.7% of the variations

323   in binned $ln(r_e)$ can be explained by the joint changes of the binned $ln(N_{CCN,0.2\%})$ and $ln(\text{PWV}_{\text{BL}})$.

324   This indicates that in the bulk part, r_e decreases with increasing $N_{CCN,0.2\%}$ and enlarges with increasing

325   PWV_{BL}. Notice that in the lower $N_{CCN,0.2\%}$ bins (<150 cm^{-3}) where the PWV_{BL} values are the lowest

326   among all the bins ($0.76 - 0.85$ cm), the limitation of cloud droplet growth by competing for the available

327   water vapor is evident by the changes in N_c and r_e. For example, the $N_{CCN,0.2\%}$ changes from 47 to 128

328   cm^{-3}, the N_c increases from 37 to 71 cm^{-3} and r_e only increases from 9.30 to 9.74 µm. In other words,

329   nearly tripling the CCN loading leads to roughly doubling N_c, while the r_e is only enlarged by 0.44 µm

330   (4.7%). In the relatively low available PWV_{BL} regime, it is clear that even with more CCN being

331   converted into cloud droplets, the limited water vapor condition prohibits the further diffusional growth

332   of those cloud droplets. However, in the higher $N_{CCN,0.2\%}$ bins (>150 cm^{-3}) with relatively higher

333   PWV_{BL}, the binned r_e values fluctuate and decrease with increasing CCN bins under similar PWV_{BL} (i.e.,

334   the two $N_{CCN,0.2\%}$ ranges from 200-400 cm^{-3}, and from 400-500 cm^{-3}). Since r_e essentially represents

335   the area-weighted information of the cloud droplet size distribution (DSD), this sorting method of r_e

336   inevitably entangles multiple cloud droplet evolution processes and environmental effects that can alter

337   the DSD, especially under the condition of sufficient water supply. Therefore, the further assessment of

338   the r_e responses to the $N_{CCN,0.2\%}$ loading under the constraint of water vapor should be discussed in order

339   to untangle the impacts of different processes and environmental effects on r_e.

340

341   **3.3 Aerosol-cloud interaction under different water vapor availabilities**

342   As previously discussed above and suggested by earlier studies, the conditions of water vapor

343   supply have a substantial impact on various processes from CCN-N_c conversion to in-cloud droplet

344   condensational growth and coalescence processes, hence effectively altering the cloud DSD (Feingold et

345   al., 2006; McComiskey et al., 2009; Zheng et al., 2020). Moving forward to examine how r_e responds to

346   the changes of $N_{CCN,0.2\%}$ in the context of given water vapor availability, an index describing the aerosol-

347   cloud interaction process is introduced as follows:

348   $$\text{ACI}_r = -\left.\frac{\partial ln(r_e)}{\partial ln(N_{CCN,0.2\%})}\right|_{\text{PWV}_{\text{BL}}}. \tag{3}$$

349   The ACI_r represents the relative change of r_e with respect to the relative change of $N_{CCN,0.2\%}$, where

350   positive ACI_r denotes the decrease of r_e with increasing $N_{CCN,0.2\%}$ under binned PWV_{BL}. This

351 assessment of ACI_r focuses on the relative sensitivity of the cloud microphysics response in the water
352 vapor stratified environment, while previous studies used the cloud liquid water path (LWP) as the
353 constraint (Twomey, 1977; Feingold et al., 2003; Garrett et al., 2004). LWP describes the liquid water
354 (i.e., existing cloud droplets) physically linked to r_e and N_c which have an interdependent relationship
355 in cloud retrieval procedures, and hence to a certain extent, share co-variabilities with cloud
356 microphysical properties (Dong et al., 1998; Wu et al., 2020a). In this study, by using the PWV as a
357 sorting variable, we are trying to capture the role of ambient available water vapor in the cloud droplet
358 growth process (especially the water vapor diffusional growth), using measurement independent to the
359 cloud retrievals. Fig. 3 shows the variation of ACI_r under different PWV_{BL} bins, and illustrates the
360 calculation of ACI_r in three different PWV_{BL} ranges. Note that in Fig. 3a, the regressions are derived
361 from all points (statistically significant with a confidence level of 95%). As shown in Fig. 3a, the ACI_r
362 values range from close-to-zero values (-0.01) to 0.22, with the mean value of 0.117 ± 0.052. The ACI_r
363 range of this study agrees well with the previous studies of MBL cloud aerosol-cloud interactions
364 (McComiskey et al., 2009; Pandithurai et al., 2009; Liu et al., 2016). It is noteworthy that the variation
365 of ACI_r with PWV_{BL} suggests two different relationships under separated PWV_{BL} conditions, as
366 discussed in the following two paragraphs.

367 Under the relatively lower PWV_{BL} condition (<1.2 cm), the low values of ACI_r (-0.01 - 0.057)
368 indicate that r_e is less sensitive to $N_{CCN,0.2\%}$, and the dependence on PWV_{BL} is also insignificant given
369 by the flat regression line (green dashed line) and low correlation coefficient of 0.38 (Fig. 3a). As
370 discussed in section 3.2, the limited water vapor can weaken the ability of condensational growth of the
371 cloud droplet converted from CCN, that is, the increase of CCN loading cannot be effectively reflected
372 by a decrease in r_e. For example, a 307% increase of $N_{CCN,0.2\%}$ only leads to a 10% decrease in r_e in the
373 PWV_{BL} range of 0.8-1.0 cm as shown in Fig. 3b. So that in this regime, even with a slight PWV_{BL} increase,
374 the lack of a sufficient amount of large cloud droplets is favorable to the predominant condensational
375 growth process, which effectively narrows the cloud DSD and, in turn, confines the variable range of r_e
376 with respect to $N_{CCN,0.2\%}$ (Pawlowska et al., 2006; Zheng et al., 2020). In this situation, the abilities of
377 CCN to cloud droplet conversion and the droplet condensational growth are limited by insufficient water
378 vapor, rather than an influx of CCN.

379 However, under the relatively higher PWV_{BL} regime (>1.2 cm), the ACI_r values become more
380 positive and express a significant increasing trend with PWV_{BL} (correlation coefficient of 0.83, blue
381 dashed line), which indicates that r_e is more susceptible to $N_{CCN,0.2\%}$ in this regime. On the one hand,
382 due to the sufficient water vapor supply, the enhanced condensational growth process allows more CCN

383   to grow into cloud droplets, so that the limiting factor of the droplet growth corresponds to the changes

384   in CCN loading. On the other hand, the increased N_c values associated with higher water vapor supply

385   in the cloud effectively enhance the coalescence process. This results in broadening the cloud DSD and

386   increasing the variation range of r_e in response to the changes of $N_{CCN,0.2\%}$. To test our hypothesis of

387   active coalescence under higher water vapor conditions, Table 2 lists the occurrence frequencies of large

388   r_e values (> 12 and 14 µm) under the six high PWV$_{BL}$ bins (1.2 – 2.4 cm), because this range of 12-14

389   µm can serve as the critical demarcation of an efficient coalescence process (Gerber, 1996; Freud and

390   Rosenfeld, 2012; Rosenfeld et al., 2012). As listed in Table 2, for the six high PWV$_{BL}$ bins, the

391   occurrence frequencies of r_e>12 µm are 25.0%, 30.6%, 54.1%, 74.2%, 93.8% and 97.5%, and the

392   occurrence frequencies of r_e>14 µm are 1.25%, 1.77%, 7.4%, 17.7%, 31.9% and 20.1%, respectively.

393   The increasing trends of large r_e occurrences mimic the trend of ACI$_r$ and suggest that with

394   increased PWV$_{BL}$, cloud droplets have a greater chance to grow via the effective coalescence process

395   and subsequently lead to an enlargement of ACI$_r$. Although previous studies have brought up the

396   potential impacts of the cloud droplet coalescence process on ACI, it is rarely seen that the relationship

397   among them has been discussed in detail. Here we provide possible explanations on how the enhanced

398   coalescence process can enlarge ACI$_r$. Quantitatively, ACI$_r$ is described by the log partial derivative ratio

399   of r_e to $N_{CCN,0.2\%}$, thus a sharper decrease of r_e with respect to a given $N_{CCN,0.2\%}$ range can result in a

400   steeper slope and in turn, larger ACI$_r$ (i.e., a 239% increase in $N_{CCN,0.2\%}$ leads to a r_e decrease of 48% in

401   the 2.2-2.4 cm bin in Fig. 3b). Physically, this relies on how the cloud droplet size distribution (DSD)

402   would change with different CCN loadings. Therefore, particularly in low CCN conditions, sufficient

403   water vapor availability will allow cloud droplets to continuously grow via diffusion of water vapor (i.e.,

404   condensational growth), and enter the active cloud-droplet coalescence regime. In contrast, the increase

405   in cloud droplet size can effectively reduce N_c via the process of large cloud droplets collecting small

406   droplets, and small droplets be coalesced into large droplets. Consequently, the cloud DSD becomes

407   effectively broadened toward the large tail by the coalescence, so that r_e is enlarged. With more CCN

408   available, the cloud DSD is narrowed by the enhanced condensational growth and regresses toward the

409   small tail by increasing the amount of newly converted cloud droplets which result in decreased r_e. These

410   interactions between CCNs and cloud droplets ultimately result in the broadened changeable range of r_e,

411   and in turn, the enlarged ACI$_r$.

412   In order to investigate the theoretical implication of supersaturation conditions on the aerosol-cloud

413   interaction observed here in the MBL stratiform clouds, the ACI$_r$ values are calculated with respect to

414   the surface N_{CCN} theoretically at two additional high supersaturation levels (0.5% and 1.2%), under all

PWV$_{BL}$ conditions. The results in Table 3 show that the ACI$_r$ signals are both weak and do not have significant changes under relatively lower PWV$_{BL}$ conditions, while the ACI$_r$ signals tend to strengthen with the increase of supersaturation under the relatively higher PWV$_{BL}$. Base on the Köhler theory, if the supersaturation exceeds the critical point for the given droplet, the droplet will thus experience continued growth, so theoretically the ACI should increase with the supersaturation under same aerosol number concentration. However, the observed limited water vapor cannot support this ideal droplet growth, results in weak responses of cloud droplets to aerosol intrusion. With the increase of observed water vapor, the continued growth of cloud droplets becomes more plausible, hence the high supersaturation yields larger droplets with low number of aerosols, more efficient droplet activation with a large number of aerosols, and in turns, larger ACI$_r$ (even out of the theoretical bounds). However, considering these high supersaturation environments are unphysical in the observed MBL cloud layers, and estimating the real supersaturation conditions using ground-based remote-sensing is beyond the scope of this study, we chose the supersaturation level of 0.2% because it represents the most typical supersaturation conditions of MBL stratiform clouds.

3.4 The co-variabilities of the meteorological factors

The environmental conditions over the ENA have been widely studied as not independent but entangled with each other (Wood et al., 2015; Zheng et al., 2016; Wu et al., 2017; Wang et al., 2021). To better understand the dependencies and the co-variabilities of the meteorological factors, a principal component analysis (PCA) is performed targeting on the following variables: (1) PWV$_{BL}$ denotes the water vapor availabilities within the boundary layer; (2) D_i describes the boundary layer coupling conditions; (3) TKE$_w$ represents the strength of boundary layer turbulence; (4) $W_{dir,NS}$ reflects the surface wind directions in terms of northerly and southerly; and (5) LTS infers the large-scale thermodynamic structures. Note that the $W_{dir,NS}$ are taken as $W_{dir,NS} = abs(W_{dir} - 180°)$, so that the original W_{dir} (0-360°) can be transformed to $W_{dir,NS}$ (0-180°) where the values smaller than 90° are close to the southerly wind, and those greater than 90° are close to the northerly wind. The $W_{dir,ns}$ are transformed as such to capture the island effects better, because the cliff is located north of the ENA site.

The input data metric is constructed from the above five variables to apply the PCA, and the principal components (PCs) that serving to explain the variation of those dependent variables can be output from the eigenanalysis. The result shows that for the five selected meteorological factors, the proportions of the total intervariable variance explained by the PCs are 43.72%, 22.01%, 18.26%, 8.95% and 7.06%, and the eigenvalues are 2.19, 1.10, 0.91, 0.45, and 0.35, respectively. Note that the first three

PCs have the highest eigenvalues and explain most (~84%) of the total variance, which indicates that they can capture the significant variation patterns of the selective meteorological factors.

To determine the relative contributions of the variables to PCs, all the five selected meteorological variables are projected to the first three PCs and the Pearson correlation coefficients between them are listed in Table 4. For the first PC (PC1) which accounts for the highest proportion (43.72%) of the total variance, the PC1 is strongly negatively correlated with PWV_{BL} (-0.84) and D_i (-0.73), but strongly positively correlated with TKE_w (0.69). These results suggest that PC1 mainly represents the boundary layer conditions, and the co-variations of the boundary layer water vapor and turbulence are the most distinct environmental patterns for the selected cloud cases. The PC2 and PC3 are most correlated with LTS (0.58 and 0.65 for PC2 and PC3, respectively) and $W_{dir,NS}$ (0.60 and -0.50 for PC2 and PC3, respectively), indicating that the PC2 and PC3 mainly describe the variations in large-scale thermodynamic and the surface wind patterns, which are likely associated with the variations of the Azores High position and strength (Wood et al., 2015).

To further understand the correlations between the meteorological variables, the principal component loadings plot is constructed by projecting the variables onto PC1 and PC2 as shown in Fig. 4. Each point denotes the variable correlations with PC1 (x-coordinate) and PC2 (y-coordinate), so that each vector represents the strength and direction of the original variable influences on the pair of PCs. The angle between the two vectors represents the correlation between each other. In Fig. 4, both TKE_w and $W_{dir,NS}$ vectors are located in the same quadrant (positive in both PC1 and PC2) and close to each other with a small degree of an acute angle, which means the TKE_w are strongly correlated with the $W_{dir,NS}$. When the surface wind is coming from the north side of the island, the topographic lifting effect of the cliff would induce additional updraft over the ENA site (Zheng et al., 2016), so that the wind closer to the northerly wind (larger $W_{dir,NS}$) is more correlated with higher TKE_w. Note that TKE_w and D_i vectors are almost in an opposite direction, which denotes a strongly negative correlation between the two variables. The angles of PWV_{BL} with D_i (~45°) and TKE_w (~142°) suggest that PWV_{BL} is moderately positively correlated with D_i but negatively correlated with TKE_w. A higher D_i indicates a more decoupled MBL, where MBL is not well-mixed and separated into a radiative-driven layer and a surface flux driven layer that caps the surface moisture (Jones et al., 2011). This situation is more likely to associate with a relatively higher PWV_{BL} and weaker TKE_w condition. As for the LTS parameter, the close to 90° angle with TKE_w suggests no correlation between them, since the LTS is mostly capturing the large-scale thermodynamical structures and is obtained from a coarser temporal resolution. Thus, the LTS does not essentially have correspondence to the strength of boundary layer turbulence and can be

479 treated as independent to TKE_w over the ENA site. The loading plot intuitively tells us the directions and

480 strengths of the co-variabilities of the selected meteorological variables, and sheds the light on

481 determining the key factors that are feasible to use in examining the environmental impacts on the

482 aerosol-cloud interactions.

483

484 **3.5 Linking the meteorological factors to aerosol-cloud interaction**

485

486 **3.5.1 Relations of meteorological factors with aerosol and cloud properties**

487 The PCs are, mathematically, the linear combination of the selected variables, and hence

488 independent of each other after the PCA. Therefore, treating the aerosol and cloud properties as

489 dependents and correlated with the PCs allows us to infer their co-variation with the meteorological

490 factors statistically. A weakly negative correlation between $N_{CCN,0.2\%}$ and PC1 ($R_{PC1,CCN} = -0.35$)

491 suggests that the relatively higher $N_{CCN,0.2\%}$ could be sometimes found under higher PWV_{BL} and lower

492 TKE_w. Though the correlation is low, the plausible contributions could come from the seasonal variations

493 of $N_{CCN,0.2\%}$ and PWV_{BL} as discussed in the previous section, and the weaker TKE_w might prevent the

494 vertical mixing of CCN and induce higher surface $N_{CCN,0.2\%}$. On the other hand, a weakly positive

495 correlation between $N_{CCN,0.2\%}$ and PC2 ($R_{PC2,CCN} = 0.21$) suggests that there are no fundamental

496 relationships between CCN with thermodynamic and the surface wind direction, and they are not the key

497 controlling factor of surface $N_{CCN,0.2\%}$ variation because the surface CCN concentration is primarily

498 contributed by the accumulation-mode aerosols which come from the condensational growth of Aitken-

499 mode aerosols (Zheng et al., 2018). As for the cloud properties, both N_c and f_{ad} are negatively correlated

500 with PC1 ($R_{PC1,Nc} = -0.51$ and $R_{PC1,fad} = -0.62$, respectively), suggesting a moderate relationship

501 between N_c, f_{ad}, and the boundary layer condition. Moreover, their low correlations with PC2

502 ($R_{PC2,Nc} = -0.10$ and $R_{PC2,fad} = -0.17$, respectively) indicate very weak relations with the large-scale

503 thermodynamic variables. Note that the same sign of correlations with PC1 statistically inferring the

504 similar directional co-variation of $N_{CCN,0.2\%}$, N_c, and f_{ad} to a certain extent.

505 To examine the physical relation between $N_{CCN,0.2\%}$, N_c and f_{ad}, the profiles of cloud r_e and

506 LWC are plotted in normalized height from cloud base (z_b) to cloud top height (z_t) (Fig. 5), which is

507 given by $z_n = (z - z_b) / (z_t - z_b)$. The solid lines denote the mean values, and the shaded area

508 represents one standard deviation at each normalized height z_n. The normalized r_e increases from ~8.6

509 μm at the cloud base toward ~11 μm near the upper part of the cloud where z_n is 0.7 (Fig. 5a), through

510 condensational growth and coalescence processes, and then decreases toward the cloud top due to cloud-

16

top entrainment. Similar in-cloud vertical variation of r_e is also found by previous study using aircraft in-situ measurements (Zhao et al., 2018; Wu et al. 2020a). Profiles of retrieved LWC and calculated adiabatic LWC_{ad} (blue line) are presented in Fig. 5b. As demonstrated in Fig. 5b, the f_{ad} values, which is the ratio of LWC to LWC_{ad}, reach a maximum of 0.8 at the cloud base and a minimum of 0.38 at the cloud top. The shaded areas of r_e and LWC denote the range from near-adiabatic to sub-adiabatic cloud environments, where in the near-adiabatic cloud (higher f_{ad}) the cloud droplets experience adiabatic growth and LWC should close to LWC_{ad}. In contrast, in the sub-adiabatic cloud regime, the decrease of f_{ad} is largely due to cloud-top entrainment and coalescence processes even in non-precipitating MBL clouds (Wood, 2012; Braun et al., 2018; Wu et al. 2020b). Furthermore, to understand the implication of cloud adiabaticity with respect to CCN-N_c conversion, all of the f_{ad} samples are separated into two groups by the median value of the layer-mean f_{ad} (0.66) for a further analysis.

Figure 6 shows N_c against the binned $N_{CCN,0.2\%}$ for the near-adiabatic regime ($f_{ad} > 0.66$) and sub-adiabatic regime ($f_{ad} < 0.66$). For the near-adiabatic regime, N_c increases from ~60 cm^{-3} to 119 cm^{-3} with increased $N_{CCN,0.2\%}$ and PWV$_{BL}$, and both $N_{CCN,0.2\%}$ and PWV$_{BL}$ appear to play positive roles in terms of the N_c increase. The result is as expected because the process of condensational growth is predominant in the near-adiabatic clouds, that is, with increasing water vapor supply, the higher CCN loading can effectively lead to more cloud droplets. However, in the sub-adiabatic cloud regime, N_c increases with increased $N_{CCN,0.2\%}$ but possesses a negative correlation with PWV, which results in a slower increase of N_c under higher $N_{CCN,0.2\%}$ and PWV$_{BL}$ conditions. The mean reduction of N_c in the sub-adiabatic regime is computed to be ~37% compared to that for the near-adiabatic clouds. As previously studied, the coalescence process contributes significantly to N_c depletion, even in a non-precipitating MBL clouds (Feingold et al., 1996; Wood, 2006). Thus, lower N_c in the sub-adiabatic regime may be partly due to the combined effect of coalescence and entrainment (Wood, 2006; Hill et al., 2009; Yum et al., 2015; Wang et al., 2020). Note that the retrieved N_c is representing the cloud layer-mean information. In summary, the Wu et al. (2020a) retrieval works as separating the reflectivity to the contributions of cloud (Z_c) and drizzle, the cloud procedure assumes an initial guess of the representative layer-mean N_c based on the climatology over ENA sites (Dong et al., 2014), and such allows the first guess of the vertical profile of LWC based on N_c and Z_c, and then constrains back the N_c and LWC using the LWP from MWR, finally output r_e (Fig.3 in Wu et al., 2020a). Therefore, the final retrieved N_c is updated to in response to the cloud microphysical processes within this time-step. From the aircraft in-situ measurements during the ACE-ENA, we used the in-situ measurement during ACE-ENA to validate the retrieval outputs and found that the observed N_c profile is near-constant in middle part of the cloud,

543 with the signal of entrainment-induced depletion near the cloud top, even in the drizzling cloud where

544 the collision-coalescence processes are more active (Wu et al., 2020a). However, it is hard and beyond

545 the scope of the ground-based retrieval to compare the vertical dependency of depletion rate within one

546 time-step. Therefore, as the retrieval currently work as representing the layer-mean information from the

547 given time-step, the preferred method in this study is to compare N_c at different times, where in this case

548 are the adiabatic versus sub-adiabatic conditions which hence yields different N_c that we retrieved from

549 the ground-based snapshot perspective. From the PCA and binning analysis, the effect of cloud

550 adiabaticities on CCN-N_c conversions may shed light on interpreting the aerosol-cloud interaction under

551 different environmental effects.

552

553 **3.5.2 The role of meteorological factors on ACI_r assessment**

554 Since ACI_r can only be calculated by the logarithmic derivatives from a set of $N_{CCN,0.2\%}$ and r_e

555 data within a certain regime, it will be inappropriate to linearly correlate the data with PCs directly, in

556 both mathematical and physical perspectives. Therefore, the meteorological factors which have the

557 strongest influence on the most explanatory PCs, namely PWV_{BL} and TKE_w are selected to be the sorting

558 variables in assessing the environmental impacts on the ACI_r. In addition, LTS is also selected as it

559 represents the large-scale thermodynamic factor and is independent to the boundary-layer environment

560 conditions. The data samples are first separated into two regimes using the median values of the targeting

561 factors, and then separated into four quadrants by the median PWV_{BL} because ACI_r is found to have

562 significant differences under different water vapor availabilities. The ACI_r values are further calculated

563 for all quadrants to examine whether the ACI_r can be distinguished by the targeting factors.

564 Combining LTS and PWV_{BL} as sorting variables, the ACI_r values for four regimes are shown in

565 Fig. S4. The ACI_r differences between low and high PWV_{BL} regimes are still retained. In the low PWV_{BL}

566 regime, the ACI_r values are limited to 0.016 and 0.056 for low and high LTS regimes, respectively. In

567 the high PWV_{BL} regime, the ACI_r values are 0.150 and 0.171 for low and high LTS regimes, respectively,

568 which is about 3-5 times greater than those in low PWV_{BL} regime. However, the ACI_r in different LTS

569 regimes cannot be distinctly differentiated (ACI_r differences between LTS regimes are ~0.02 and ~0.04),

570 and the main difference in ACI_r are still induced by the PWV_{BL}. Owing to the location of the ENA site

571 where it locates near the boundary of mid-latitude and subtropical climate regimes, the MBL clouds over

572 the ENA are found to be often under the influences of cold fronts associated with mid-latitude cyclones,

573 where the cloud evolutions are subject to the combine effects of post-frontal and large-scale subsidence

574 (Wood et al., 2015; Zheng et al., 2020; Wang et al., 2021). Therefore, over the ENA, although the spatial

575 gradient of LTS is studied to be associated with the production of MBL turbulence and the change in

576 wind direction (Wu et al., 2017), the LTS value itself is examined to has a weak impact on the aerosol-

577 cloud interaction from this study.

578   The TKE_w has been found to be strongly positively correlated with $W_{dir,NS}$ and negatively

579 correlated with D_i from the PCA, that is, the values of TKE_w already account for the co-variabilities in

580 these variables. Therefore, treating TKE_w as the sorting variable would lead to a more physical process-

581 orientated assessment. Accordingly, to examine the role of the dynamical factors on ACI, the samples

582 are separated into four regimes demarcated by the median values of PWV_{BL} and TKE_w (Fig. 7), and the

583 mean values of D_i and f_{ad} in the four quadrants are also displayed in Fig. 7. The effect of PWV_{BL} on

584 ACI_r is demonstrated by the mean ACI_r values where they are much higher in the high PWV_{BL} regime

585 than those in the low PWV_{BL} regime no matter what the TKE_w regimes. Furthermore, the result illustrates

586 that TKE_w does play an important role in ACI_r, because the ACI_r values in the high TKE_w regime are

587 more than double than the values in the low TKE_w regime.

588   In the regimes of high TKE_w and PWV_{BL}, which are closely associated with coupled MBL ($D_i =$

589 0.21) and more sub-adiabatic cloud conditions ($f_{ad} = 0.52$), r_e is highly sensitive to CCN loading with

590 the highest ACI_r of 0.259. The sufficient water vapor availability allows CCN to be converted into cloud

591 droplets more effectively, while the relatively higher TKE_w indicates stronger turbulence in the below-

592 cloud boundary layer and maintains a nearly well-mixed MBL. The CCN and moisture below-cloud layer

593 are efficiently transported and mixed aloft via the ascending branch of the eddies (Nicholls, 1984; Hogan

594 et al., 2009), hence are effectively connected to the cloud layer. Therefore, under the lower CCN loading

595 condition, the active coalescence process (which indicated by the low f_{ad} values) results in the depletion

596 of small cloud droplets and broadening of cloud DSD (Chandrakar et al., 2016), and in turn, leads to

597 further enlarged r_e. However, with higher CCN intrusion into the cloud layer, the enhanced cloud droplet

598 conversion and the subsequential condensational growth behave contradictorily to narrow the DSD

599 (Pinsky and Khain, 2002; Pawlowska et al., 2006), which leads to decreased r_e. Therefore, the MBL

600 clouds are distinctly susceptible to CCN loading under the environments of sufficient water vapor and

601 strong turbulence in which the ACI_r is enlarged.

602   Under high PWV_{BL} but low TKE_w conditions, the mean ACI_r reduces to 0.101 (~ 39% of that

603 under high TKE_w). The MBL is more likely decoupled where $D_i = 0.54$, which indicates that the weaker

604 turbulence loosens the connection between the cloud layer and the underlying boundary layer. This

605 results in a less effective conversion of CCN into cloud droplets, while the more adiabatic cloud

606 environment ($f_{ad} = 0.75$) denotes the lack of coalescence growths and thus diminishes the r_e sensitivity

607 to CCN. Although the constraints of insufficient water vapor on ACI_r are still evident, the ACI_r values
608 increase from 0.008 in the low TKE_w regime to 0.024 in the high TKE_w regime. The ACI_r differences
609 between the two TKE_w regimes attest that ACI_r strongly depends on the connection between the cloud
610 layer and the below-cloud boundary layer CCN and moisture, that is, stronger turbulence can enhance
611 the susceptibility of r_e to CCN.

612   In this study, the relationship between turbulence and ACI is found to be valid in non-precipitating
613 MBL clouds. Theoretically, the effect of turbulence on ACI_r would appear to be artificially amplified, if
614 in the presence of precipitation. The intensive turbulence can enhance the coalescence process and
615 accelerate the CCN-cloud cycling, and subsequently, the CCN depletion due to precipitation and
616 coalescence scavenging would result in quantitatively enlarged ACI_r (Feingold et al., 1996, 1999; Duong
617 et al., 2011; Braun et al., 2018). Though it is beyond the scope of this study, it would be of interest to
618 perform such analysis on the aerosol-cloud-precipitation interaction using ground-based remote sensing
619 and model simulations in the future study.

620

621 **4. Summaries and Conclusions**

622   Over the ARM-ENA site, a total of 20 non-precipitating single-layered MBL stratus and
623 stratocumulus cloud cases have been selected in order to investigate the aerosol-cloud interaction (ACI).
624 The distributions of CCN and cloud properties for selected cases represent the typical characteristics of
625 non-precipitating MBL clouds in a relatively clean environment over the remote oceanic area. The
626 diversity of boundary layer conditions and cloud adiabaticities among the selected cases enable the
627 investigation of different environmental effects on ACI.

628   The overall variations of N_c with $N_{CCN,0.2\%}$ show an increasing trend, regardless of the water vapor
629 condition, while the sufficient PWV_{BL} appears to stabilize the CCN-N_c conversion process. The water
630 vapor limitation on cloud droplet growth is evident in the lower $N_{CCN,0.2\%}$ up to 150 cm^{-3} with low
631 PWV_{BL} values, where a near tripling of CCN loading leads to a near doubling of N_c but only 4.7%
632 increase in r_e. When $N_{CCN,0.2\%}$ is greater than 250 cm^{-3} and PWV_{BL} values are also relatively high, r_e
633 appears to decrease with increasing $N_{CCN,0.2\%}$ under similar water vapor conditions. As for bulk aerosol-
634 cloud interaction, the ACI_r values vary from -0.01 to 0.22 for different PWV_{BL} conditions where ACI_r
635 appears to be diminished under limited water vapor availability due to the limited droplet activation and
636 condensational growth process. While under relatively sufficient water supply condition, r_e shows more
637 sensitive responses to the changes of $N_{CCN,0.2\%}$, due to the combined effect of condensational growth and
638 coalescence processes accompanying the higher N_c and PWV_{BL}.

639   The theoretical diagram describing the mechanism proposed above is shown in Fig. 8. Under the
640   relatively lower PWV$_{BL}$ condition, the limited water vapor weakens the ability of condensational growth
641   of the cloud droplet converted from CCN, which results in both less newly converted as well as large
642   cloud droplets, with the lack of chance of coalescence process under this circumstance. Therefore, the
643   variable range of r_e versus $N_{CCN,0.2\%}$ is narrowed and presented as small ACI$_r$. While under the relatively
644   higher PWV$_{BL}$ condition, particularly in low CCN conditions, the sufficient water vapor availability
645   allows cloud droplets growing via the condensation of water vapor, and thus enter the active cloud-
646   droplet coalescence regime. In contrast, the increase in cloud droplet size can effectively reduce N_c via
647   the coalescence process and the size distributions are effectively broadened toward the large tail by the
648   coalescence, so that r_e is enlarged. Under a higher $N_{CCN,0.2\%}$ intrusion, the cloud droplet size distribution
649   is narrowed by the enhanced condensational growth and regresses toward the small tail by increasing the
650   amount of newly converted cloud droplets which results in decreased r_e. Combinedly, the interactions
651   between CCNs and cloud droplet growing processes ultimately result in a broadened changeable range
652   of r_e, and in turn, the enlarged ACI$_r$.

653   The co-variabilities among the environmental factors are examined using the multi-dimensional
654   PCA. The variables of PWV$_{BL}$, D_i, TKE$_w$, LTS and $W_{dir,NS}$ are constructed as the input of the
655   eigenanalysis. Results show that the first three PCs can describe the majority (~84%) of the variance
656   among the selected variables. The most explanatory PC1 (account for 43.72% contribution) strongly
657   correlated with PWV$_{BL}$, D_i (both negatively) and TKE$_w$ (positively), and hence describe the co-variation
658   of the boundary layer conditions. While the PC2 and PC3 (account for 22.01% and 18.26% contributions,
659   respectively) are strongly correlated with LTS and $W_{dir,NS}$, which likely indicates the variations of the
660   Azores High position and strength. By projecting the variables onto PC1 and PC2, the PCA loading
661   analysis shows that TKE$_w$ is strongly negatively correlated with D_i, which is what we expected. A
662   decoupled MBL cloud is often separated into two layers where the lower one can cap the surface moisture,
663   while the higher TKE$_w$ denote sufficient turbulence that maintains the well-mixed MBL. Additionally,
664   the island effect is also indicated by the eigenanalysis, where surface northerly wind would induce
665   additional updraft velocity and hence disturb TKE$_w$, owing to the topographic effect of the cliff north of
666   the ENA site. The role of cloud adiabaticities on the behaviors of CCN-N_c conversion is examined using
667   both binning and eigenanalysis. In a near-adiabatic cloud vertical structure, the cloud droplet growing
668   process is dominated by condensational growth, thus the N_c responses to increased $N_{CCN,0.2\%}$ and
669   PWV$_{BL}$ are strengthened. When the cloud layer becomes more sub-adiabatic, the effect of coalescence
670   leads to the depletion of N_c and thus results in the lower retrieved N_c from a ground-based snapshot

671 perspective. The competition between the condensational growth and coalescence processes strongly
672 impacts the variations of cloud microphysics to CCN loading.

673   To investigate the environmental effects on ACI_r, the factors having the most influence on the
674 explanatory PCs are selected as the sorting variables in the ACI_r assessments. The LTS sorting method
675 cannot distinguish the ACI_r values, which means the LTS values themselves have a weak impact on ACI_r
676 due to the MBL cloud cover over the ENA is mainly impacted by the mid-latitude cyclone systems. In
677 contrast, the intensity of boundary layer turbulence represented by TKE_w plays a more important role in
678 ACI_r, since the values of TKE_w already account for the co-variations of the MBL conditions, and hence
679 leads to a physical process-orientated assessment. The ACI_r assessments in four different TKE_w and
680 PWV_{BL} regimes show that the constraints of insufficient water vapor on the ACI_r are still evident, but in
681 both PWV_{BL} regimes the ACI_r values increase more than double from low TKE_w to high TKE_w regimes.
682 Noticeably, the ACI_r increases from 0.101 in the low TKE_w regime to 0.259 in the high TKE_w regime,
683 under high PWV_{BL} conditions. The intensive below-cloud boundary layer turbulence strengthens the
684 connection between the cloud layer and below-cloud CCN and moisture. So that with sufficient water
685 vapor, an active coalescence leads to further enlarged r_e, particularly for low CCN loading condition,
686 while the enhanced N_c from condensational growth induced by increased $N_{CCN,0.2\%}$ can effectively
687 decrease r_e. Combining these processes together, the enlarged ACI_r is presented.

688   In this study, the non-precipitating MBL clouds are found to be most susceptible to the below-cloud
689 CCN loading under environments with sufficient water vapor and stronger turbulence. This study
690 examines the importance of the environmental effects on the ACI_r assessments, and provides the
691 observational constraints to the future model evaluations on the aerosol-cloud interactions. Future studies
692 will be focusing on exploring the role of environmental effects on the aerosol-cloud-precipitation
693 interactions in MBL stratocumulus through an integrative analysis of observations and model simulations.
694
695

721

References.

Albrecht, B. A., Bretherton, C. S., Johnson, D., Schubert, W. H. and Frisch, A. S.: The Atlantic Stratocumulus Transition Experiment - ASTEX, Bull. - Am. Meteorol. Soc., doi:10.1175/1520-0477(1995)076<0889:TASTE>2.0.CO;2, 1995.

ARM MET Handbook: ARM Surface Meteorology Systems (MET) Handbook, DOE ARM Climate Research Facility, DOE/SC-ARM/TR-086. Available at: https://www.arm.gov/publications/tech_reports/handbooks/met_handbook.pdf, last access: 21 August 2021.

Braun, R. A., Dadashazar, H., MacDonald, A. B., Crosbie, E., Jonsson, H. H., Woods, R. K., Flagan, R. C., Seinfeld, J. H. and Sorooshian, A.: Cloud Adiabaticity and Its Relationship to Marine Stratocumulus Characteristics Over the Northeast Pacific Ocean, J. Geophys. Res. Atmos., doi:10.1029/2018JD029287, 2018.

734 Cadeddu, M. P., Liljegren, J. C. and Turner, D. D.: The atmospheric radiation measurement (ARM)
735   program network of microwave radiometers: Instrumentation, data, and retrievals, Atmos. Meas.
736   Tech., doi:10.5194/amt-6-2359-2013, 2013.

737 Chandrakar, K. K., Cantrell, W., Chang, K., Ciochetto, D., Niedermeier, D., Ovchinnikov, M., Shaw, R.
738   A. and Yang, F.: Aerosol indirect effect from turbulence-induced broadening of cloud-droplet size
739   distributions, Proc. Natl. Acad. Sci. U. S. A., doi:10.1073/pnas.1612686113, 2016.

740 Chen, Y. C., Christensen, M. W., Stephens, G. L. and Seinfeld, J. H.: Satellite-based estimate of global
741   aerosol-cloud radiative forcing by marine warm clouds, Nat. Geosci., doi:10.1038/ngeo2214, 2014.

742 Costantino, L. and Bréon, F. M.: Analysis of aerosol-cloud interaction from multi-sensor satellite
743   observations, Geophys. Res. Lett., doi:10.1029/2009GL041828, 2010.

744 Diamond, M. S., Dobracki, A., Freitag, S., Griswold, J. D. S., Heikkila, A., Howell, S. G., Kacarab, M.
745   E., Podolske, J. R., Saide, P. E. and Wood, R.: Time-dependent entrainment of smoke presents an
746   observational challenge for assessing aerosol-cloud interactions over the southeast Atlantic Ocean,
747   Atmos. Chem. Phys., doi:10.5194/acp-18-14623-2018, 2018.

748 Dong, X., Xi, B., Kennedy, A., Minnis, P. and Wood, R.: A 19-month record of marine aerosol-cloud-
749   radiation properties derived from DOE ARM mobile facility deployment at the Azores. Part I: Cloud
750   fraction and single-layered MBL cloud properties, J. Clim., doi:10.1175/JCLI-D-13-00553.1, 2014.

751 Dong, X., Schwantes, A. C., Xi, B. and Wu, P.: Investigation of the marine boundary layer cloud and
752   CCN properties under coupled and decoupled conditions over the azores, J. Geophys. Res.,
753   doi:10.1002/2014JD022939, 2015.

754 Duong, H. T., Sorooshian, A. and Feingold, G.: Investigating potential biases in observed and modeled
755   metrics of aerosol-cloud-precipitation interactions, Atmos. Chem. Phys., doi:10.5194/acp-11-4027-
756   2011, 2011.

757 Fan, J., Wang, Y., Rosenfeld, D., Liu, X.: Review of Aerosol-Cloud Interactions: Mechanisms,
758   Significance and Challenges, J. Atmo. Sci. 73(11), 4221-4252, 2016.

759 Feingold, G., Kreidenweis, S. M., Stevens, B. and Cotton, W. R.: Numerical simulations of stratocumulus

760   processing of cloud condensation nuclei through collision-coalescence, J. Geophys. Res. Atmos.,

761   doi:10.1029/96jd01552, 1996.

762 Feingold, G., Frisch, A. S., Stevens, B. and Cotton, W. R.: On the relationship among cloud turbulence,

763   droplet formation and drizzle as viewed by Doppler radar, microwave radiometer and lidar, J.

764   Geophys. Res. Atmos., doi:10.1029/1999JD900482, 1999.

765 Feingold, G., Furrer, R., Pilewskie, P., Remer, L. A., Min, Q. and Jonsson, H.: Aerosol indirect effect

766   studies at Southern Great Plains during the May 2003 Intensive Operations Period, J. Geophys. Res.

767   Atmos., doi:10.1029/2004JD005648, 2006.

768 Feingold, G. and McComiskey, A.: ARM's Aerosol–Cloud–Precipitation Research (Aerosol Indirect

769   Effects), Meteorol. Monogr., doi:10.1175/amsmonographs-d-15-0022.1, 2016.

770 Freud, E. and Rosenfeld, D.: Linear relation between convective cloud drop number concentration and

771   depth for rain initiation, J. Geophys. Res. Atmos., doi:10.1029/2011JD016457, 2012.

772 Garrett, T. J. and Zhao, C.: Increased Arctic cloud longwave emissivity associated with pollution from

773   mid-latitudes, Nature, doi:10.1038/nature04636, 2006.

774 Garrett, T. J., Zhao, C., Dong, X., Mace, G. G. and Hobbs, P. V.: Effects of varying aerosol regimes on

775   low-level Arctic stratus, Geophys. Res. Lett., doi:10.1029/2004GL019928, 2004.

776 Gerber, H.: Microphysics of marine stratocumulus clouds with two drizzle modes, J. Atmos. Sci.,

777   doi:10.1175/1520-0469(1996)053<1649:MOMSCW>2.0.CO;2, 1996.

778 Ghate, V. P., Albrecht, B. A. and Kollias, P.: Vertical velocity structure of nonprecipitating continental

779   boundary layer stratocumulus clouds, J. Geophys. Res. Atmos., doi:10.1029/2009JD013091, 2010.

780 Ghate, V. P. and Cadeddu, M. P.: Drizzle and Turbulence Below Closed Cellular Marine Stratocumulus

781   Clouds, J. Geophys. Res. Atmos., doi:10.1029/2018JD030141, 2019.

782 Gryspeerdt, E., Quaas, J. and Bellouin, N.: Constraining the aerosol influence on cloud fraction, J.

783   Geophys. Res., doi:10.1002/2015JD023744, 2016.

784   Hill, A. A., Feingold, G. and Jiang, H.: The influence of entrainment and mixing assumption on aerosol–

785   cloud interactions in marine stratocumulus, J. Atmos. Sci., doi: 10.1175/2008JAS2909.1, 2009.

786   Hogan, R. J., Grant, A. L. M., Illingworth, A. J., Pearson, G. N. and O'Connor, E. J.: Vertical velocity

787   variance and skewness in clear and cloud-topped boundary layers as revealed by Doppler lidar, Q.

788   J. R. Meteorol. Soc., doi:10.1002/qj.413, 2009.

789   Hudson, J. G. and Noble, S.: CCN and Vertical Velocity Influences on Droplet Concentrations and

790   Supersaturations in Clean and Polluted Stratus Clouds, J. Atmos. Sci., doi:10.1175/jas-d-13-086.1,

791   2013.

792   Jones, C. R., Bretherton, C. S., and Leon, D.: Coupled vs. decoupled boundary layers in VOCALS-REx,

793   Atmos. Chem. Phys., 11, 7143–7153, https://doi.org/10.5194/acp-11-7143-2011, 2011.

794   Klein, S. A. and Hartmann, D. L.: The seasonal cycle of low stratiform clouds, J. Clim.,

795   doi:10.1175/1520-0442(1993)006<1587:TSCOLS>2.0.CO;2, 1993.

796   Kim, B. G., Miller, M. A., Schwartz, S. E., Liu, Y. and Min, Q.: The role of adiabaticity in the aerosol

797   first indirect effect, J. Geophys. Res. Atmos., doi:10.1029/2007JD008961, 2008.

798   Liu, J., Li, Z. and Cribb, M.: Response of marine boundary layer cloud properties to aerosol perturbations

799   associated with meteorological conditions from the 19-month AMF-Azores campaign, J. Atmos.

800   Sci., doi:10.1175/JAS-D-15-0364.1, 2016.

801   Lappen, C. L. and Randall, D. A.: Toward a unified parameterization of the boundary layer and moist

802   convection. Part I: A new type of mass-flux model, J. Atmos. Sci., doi:10.1175/1520-

803   0469(2001)058<2021:TAUPOT>2.0.CO;2, 2001.

804   Logan, T., Xi, B. and Dong, X.: Aerosol properties and their influences on marine boundary layer cloud

805   condensation nuclei at the ARM mobile facility over the Azores, J. Geophys. Res.,

806   doi:10.1002/2013JD021288, 2014.

807   Logan, T., Dong, X. and Xi, B.: Aerosol properties and their impacts on surface CCN at the ARM
808   Southern Great Plains site during the 2011 Midlatitude Continental Convective Clouds Experiment,
809   Adv. Atmos. Sci., doi:10.1007/s00376-017-7033-2, 2018.

810   Lu, M. L., Conant, W. C., Jonsson, H. H., Varutbangkul, V., Flagan, R. C. and Seinfeld, J. H.: The marine
811   stratus/stratocumulus experiment (MASE): Aerosol-cloud relationships in marine stratocumulus, J.
812   Geophys. Res., doi:10.1029/2006JD007985, 2007.

813   Mann, J. A., Christine Chiu, J., Hogan, R. J., O'Connor, E. J., L'Ecuyer, T. S., Stein, T. H. and Jefferson,
814   A.: Aerosol impacts on drizzle properties in warm clouds from ARM Mobile Facility maritime and
815   continental deployments, J. Geophys. Res., doi:10.1002/2013JD021339, 2014.

816   Martin, G. M., Johnson, D. W. and Spice, A.: The Measurement and Parameterization of Effective Radius
817   of Droplets in Warm Stratocumulus Clouds, J. Atmos. Sci., doi:10.1175/1520-
818   0469(1994)051<1823:tmapoe>2.0.co;2, 1994.

819   Martins, J. V., Marshak, A., Remer, L. A., Rosenfeld, D., Kaufman, Y. J., Fernandez-Borda, R., Koren,
820   I., Correia, A. L., Zubko, V. and Artaxo, P.: Remote sensing the vertical profile of cloud droplet
821   effective radius, thermodynamic phase, and temperature, Atmos. Chem. Phys., doi:10.5194/acp-11-
822   9485-2011, 2011.

823   McComiskey, A, Feingold, G., Frisch, A. S., Turner, D. D., Miller, M., Chiu, J. C., Min, Q. and Ogren,
824   J.: An assessment of aerosol-cloud interactions in marine stratus clouds based on surface remote
825   sensing, J. Geophys. Res., 114, D09203, doi:10.1029/2008JD011006, 2009.

826   McComiskey, A. and Feingold, G.: The scale problem in quantifying aerosol indirect effects, Atmos.
827   Chem. Phys., doi:10.5194/acp-12-1031-2012, 2012.

828   Medeiros, B. and Stevens, B.: Revealing differences in GCM representations of low clouds, Clim. Dyn.,
829   doi:10.1007/s00382-009-0694-5, 2011.

830   Morris, V. R.: Ceilometer Instrument Handbook, DOE ARM Climate Research Facility, DOE/SC-ARM-
831   TR-020,   2016.   Available   at:

https://www.arm.gov/publications/tech_reports/handbooks/ceil_handbook.pdf, last access: 23 April 2021.

Newsom, R. K., Sivaraman, C., Shippert, T.R. and Riihimaki, L. D.: Doppler Lidar Vertical Velocity Statistics Value-Added Product. DOE ARM Climate Research Facility, DOE/SC-ARM/TR-149, 2019. Available at: https://www.arm.gov/publications/tech_reports/doe-sc-arm-tr-149.pdf, last access: 2 September 2021.

Nicholls, S.: The dynamics of stratocumulus: Aircraft observations and comparisons with a mixed layer model, Q. J. R. Meteorol. Soc., doi:10.1002/qj.49711046603, 1984.

Pandithurai, G., Takamura, T., Yamaguchi, J., Miyagi, K., Takano, T., Ishizaka, Y., Dipu, S. and Shimizu, A.: Aerosol effect on cloud droplet size as monitored from surface-based remote sensing over East China Sea region, Geophys. Res. Lett., doi:10.1029/2009GL038451, 2009.

Pawlowska, H., Grabowski, W. W. and Brenguier, J. L.: Observations of the width of cloud droplet spectra in stratocumulus, Geophys. Res. Lett., doi:10.1029/2006GL026841, 2006.

Pearson, G., Davies, F. and Collier, C.: An analysis of the performance of the UFAM pulsed Doppler lidar for observing the boundary layer, J. Atmos. Ocean. Technol., doi:10.1175/2008JTECHA1128.1, 2009.

Pinsky, M. B. and Khain, A. P.: Effects of in-cloud nucleation and turbulence on droplet spectrum formation in cumulus clouds, Q. J. R. Meteorol. Soc., doi:10.1256/003590002321042072, 2002.

Qiu, Y., Zhao, C., Guo, J. and Li, J.: 8-Year ground-based observational analysis about the seasonal variation of the aerosol-cloud droplet effective radius relationship at SGP site, Atmos. Environ., doi:10.1016/j.atmosenv.2017.06.002, 2017.

Romps, D. M.: Exact expression for the lifting condensation level, J. Atmos. Sci., doi:10.1175/JAS-D-17-0102.1, 2017.

Rosenfeld, D. and Woodley, W. L.: Closing the 50-year circle: From cloud seeding to space and back to climate change through precipitation physics. Chapter 6 of "Cloud Systems, Hurricanes, and the

Tropical Rainfall Measuring Mission (TRMM)", edited by: Tao, W.-K. and Adler, R. F., Meteor. Monogr., 51, 234 pp., 59–80, AMS, 2003.

Rosenfeld, D.: Aerosol-Cloud Interactions Control of Earth Radiation and Latent Heat Release Budgets, in Solar Variability and Planetary Climates., 2007.

Rosenfeld, D., Wang, H. and Rasch, P. J.: The roles of cloud drop effective radius and LWP in determining rain properties in marine stratocumulus, Geophys. Res. Lett., doi:10.1029/2012GL052028, 2012.

Rosenfeld, D., Zhu, Y., Wang, M., Zheng, Y., Goren, T. and Yu, S.: Aerosol-driven droplet concentrations dominate coverage and water of oceanic low-level clouds, Science (80-.)., doi:10.1126/science.aav0566, 2019.

Seinfeld, J. H., Bretherton, C., Carslaw, K. S., Coe, H., DeMott, P. J., Dunlea, E. J., Feingold, G., Ghan, S., Guenther, A. B., Kahn, R., Kraucunas, I., Kreidenweis, S. M., Molina, M. J., Nenes, A., Penner, J. E., Prather, K. A., Ramanathan, V., Ramaswamy, V., Rasch, P. J., Ravishankara, A. R., Rosenfeld, D., Stephens, G. and Wood, R.: Improving our fundamental understanding of the role of aerosol-cloud interactions in the climate system, Proc. Natl. Acad. Sci. U. S. A., doi:10.1073/pnas.1514043113, 2016.

Siebert, H., Szodry, K.-E., Egerer, U., Wehner, B., Henning, S., Chevalier, K., Lückerath, J., Welz, O., Weinhold, K., Lauermann, F., Gottschalk, M., Ehrlich, A., Wendisch, M., Fialho, P., Roberts, G., Allwayin, N., Schum, S., Shaw, R. A., Mazzoleni, C., Mazzoleni, L., Nowak, J. L., Malinowski, S. P., Karpinska, K., Kumala, W., Czyzewska, D., Luke, E. P., Kollias, P., Wood, R. and Mellado, J. P.: Observations of Aerosol, Cloud, Turbulence, and Radiation Properties at the Top of the Marine Boundary Layer over the Eastern North Atlantic Ocean: The ACORES Campaign, Bull. Am. Meteorol. Soc., doi:10.1175/bams-d-19-0191.1, 2021.

Thorsen, T. J. and Fu, Q.: Automated retrieval of cloud and aerosol properties from the ARM Raman Lidar. Part II: Extinction, J. Atmos. Ocean. Technol., doi:10.1175/JTECH-D-14-00178.1, 2015.

882 Toto, T, and Jensen, M: Interpolated Sounding and Gridded Sounding Value-Added Products. DOE

883   ARM Climate Research Facility, DOE/SC-ARM-TR-183, 2016. Available at:

884   https://www.arm.gov/publications/tech_reports/doe-sc-arm-tr-183.pdf, last access: 2 September

885   2021.

886 Twohy, C. H., Petters, M. D., Snider, J. R., Stevens, B., Tahnk, W., Wetzel, M., Russell, L. and Burnet,

887   F.: Evaluation of the aerosol indirect effect in marine stratocumulus clouds: Droplet number, size,

888   liquid water path, and radiative impact, J. Geophys. Res. D Atmos., doi:10.1029/2004JD005116,

889   2005.

890 Twomey, S.: The nuclei of natural cloud formation part II: The supersaturation in natural clouds and the

891   variation of cloud droplet concentration, Geofis. Pura e Appl., doi:10.1007/BF01993560, 1959.

892 Twomey, S.: The Influence of Pollution on the Shortwave Albedo of Clouds, J. Atmos. Sci.,

893   doi:10.1175/1520-0469(1977)034<1149:TIOPOT>2.0.CO;2, 1977.

894 Wang, Y., Jiang, J.H., Su, H., Choi, S., Huang, L., Guo, J., and Yung, Y. L.: Elucidating the Role of

895   Anthropogenic Aerosols In Arctic Sea Ice Variations, J. Climate 31(1), 99-114, 2018.

896 Wang, Y., Zheng, X., Dong, X., Xi, B., Wu, P., Logan, T., and Yung, Y. L.: Impacts of long-range

897   transport of aerosols on marine-boundary-layer clouds in the eastern North Atlantic, Atmos. Chem.

898   Phys., 20, 14741–14755, https://doi.org/10.5194/acp-20-14741-2020, 2020.

899 West, R. E. L., Stier, P., Jones, A., Johnson, C. E., Mann, G. W., Bellouin, N., Partridge, D. G. and

900   Kipling, Z.: The importance of vertical velocity variability for estimates of the indirect aerosol

901   effects, Atmos. Chem. Phys., doi:10.5194/acp-14-6369-2014, 2014.

902 Widener, K, Bharadwaj, N, and Johnson, K: Ka-Band ARM Zenith Radar (KAZR) Instrument Handbook.

903   DOE ARM Climate Research Facility, DOE/SC-ARM/TR-106, 2012. Available at:

904   https://www.arm.gov/publications/tech_reports/handbooks/kazr_handbook.pdf, last access: 23

905   April 2021.

906 Wood, R.: Rate of loss of cloud droplets by coalescence in warm clouds, J. Geophys. Res. Atmos.,

907   doi:10.1029/2006JD007553, 2006.

908 Wood, R. and Bretherton, C. S.: On the relationship between stratiform low cloud cover and lower-

909   tropospheric stability, J. Clim., doi:10.1175/JCLI3988.1, 2006.

910 Wood, R.: Stratocumulus clouds, Mon. Weather Rev., doi:10.1175/MWR-D-11-00121.1, 2012.

911 Wood, R., Wyant, M., Bretherton, C. S., Rémillard, J., Kollias, P., Fletcher, J., Stemmler, J., De Szoeke,

912   S., Yuter, S., Miller, M., Mechem, D., Tselioudis, G., Chiu, J. C., Mann, J. A. L., O'Connor, E. J.,

913   Hogan, R. J., Dong, X., Miller, M., Ghate, V., Jefferson, A., Min, Q., Minnis, P., Palikonda, R.,

914   Albrecht, B., Luke, E., Hannay, C. and Lin, Y.: Clouds, aerosols, and precipitation in the marine

915   boundary layer: An arm mobile facility deployment, Bull. Am. Meteorol. Soc., doi:10.1175/BAMS-

916   D-13-00180.1, 2015.

917 Wu, P., Dong, X. and Xi, B.: Marine boundary layer drizzle properties and their impact on cloud property

918   retrieval, Atmos. Meas. Tech., doi:10.5194/amt-8-3555-2015, 2015.

919 Wu, P., Dong, X., Xi, B., Liu, Y., Thieman, M. and Minnis, P.: Effects of environment forcing on marine

920   boundary layer cloud-drizzle processes, J. Geophys. Res., doi:10.1002/2016JD026326, 2017.

921 Wu, P., Dong, X., Xi, B., Tian, J. and Ward, D. M.: Profiles of MBL Cloud and Drizzle Microphysical

922   Properties Retrieved From Ground-Based Observations and Validated by Aircraft In Situ

923   Measurements Over the Azores, J. Geophys. Res. Atmos., doi:10.1029/2019JD032205, 2020a.

924 Wu, P., Dong, X. and Xi, B.: A climatology of marine boundary layer cloud and drizzle properties

925   derived from ground-based observations over the azores, J. Clim., doi:10.1175/JCLI-D-20-0272.1,

926   2020b.

927 Xi, B., Dong, X., Minnis, P. and Khaiyer, M. M.: A 10 year climatology of cloud fraction and vertical

928   distribution derived from both surface and GOES observations over the DOE ARM SPG site, J.

929   Geophys. Res. Atmos., doi:10.1029/2009JD012800, 2010.

930 Yang, Y., Zhao, C., Dong, X., Fan, G., Zhou, Y., Wang, Y., Zhao, L., Lv, F. and Yan, F.: Toward
931   understanding the process-level impacts of aerosols on microphysical properties of shallow cumulus
932   cloud using aircraft observations, Atmos. Res., doi:10.1016/j.atmosres.2019.01.027, 2019.

933 Yue, Q., Kahn, B. H., Fetzer, E. J. and Teixeira, J.: Relationship between marine boundary layer clouds
934   and lower tropospheric stability observed by AIRS, CloudSat, and CALIOP, J. Geophys. Res.
935   Atmos., doi:10.1029/2011JD016136, 2011.

936 Yum, S. S., Wang, J., Liu, Y., Senum, G., Springston, S., McGraw, R. and Yeom, J. M.: Cloud
937   microphysical relationships and their implication on entrainment and mixing mechanism for the
938   stratocumulus clouds measured during the VOCALS project, J. Geophys. Res.,
939   doi:10.1002/2014JD022802, 2015.

940 Zhang, S., Wang, M., J. Ghan, S., Ding, A., Wang, H., Zhang, K., Neubauer, D., Lohmann, U., Ferrachat,
941   S., Takeamura, T., Gettelman, A., Morrison, H., Lee, Y., T. Shindell, D., G. Partridge, D., Stier, P.,
942   Kipling, Z. and Fu, C.: On the characteristics of aerosol indirect effect based on dynamic regimes
943   in global climate models, Atmos. Chem. Phys., doi:10.5194/acp-16-2765-2016, 2016.

944 Zhao, C., Qiu, Y., Dong, X., Wang, Z., Peng, Y., Li, B., Wu, Z. and Wang, Y.: Negative Aerosol-Cloud
945   re Relationship From Aircraft Observations Over Hebei, China, Earth Sp. Sci.,
946   doi:10.1002/2017EA000346, 2018.

947 Zhao, C., Zhao, L. and Dong, X.: A case study of stratus cloud properties using in situ aircraft
948   observations over Huanghua, China, Atmosphere (Basel)., doi:10.3390/atmos10010019, 2019.

949 Zawadowicz, M. A., Suski, K., Liu, J., Pekour, M., Fast, J., Mei, F., Sedlacek, A., Springston, S., Wang,
950   Y., Zaveri, R. A., Wood, R., Wang, J., and Shilling, J. E.: Aircraft measurements of aerosol and
951   trace gas chemistry in the Eastern North Atlantic, Atmos. Chem. Phys. Discuss. [preprint],
952   https://doi.org/10.5194/acp-2020-887, in review, 2020.

953 Zheng, G., Wang, Y., Aiken, A. C., Gallo, F., Jensen, M. P., Kollias, P., Kuang, C., Luke, E., Springston,
954   S., Uin, J., Wood, R., and Wang, J.: Marine boundary layer aerosol in the eastern North Atlantic:

seasonal variations and key controlling processes, Atmos. Chem. Phys., 18, 17615–17635, https://doi.org/10.5194/acp-18-17615-2018, 2018.

Zheng, G., Kuang, C., Uin, J., Watson, T., and Wang, J.: Large contribution of organics to condensational growth and formation of cloud condensation nuclei (CCN) in the remote marine boundary layer, Atmos. Chem. Phys., 20, 12515–12525, https://doi.org/10.5194/acp-20-12515-2020, 2020.

Zheng, X., Xi, B., Dong, X., Logan, T., Wang, Y. and Wu, P.: Investigation of aerosol-cloud interactions under different absorptive aerosol regimes using Atmospheric Radiation Measurement (ARM) southern Great Plains (SGP) ground-based measurements, Atmos. Chem. Phys., doi:10.5194/acp-20-3483-2020, 2020.

Zheng, Y., Rosenfeld, D. and Li, Z.: Quantifying cloud base updraft speeds of marine stratocumulus from cloud top radiative cooling, Geophys. Res. Lett., doi:10.1002/2016GL071185, 2016.

Zheng, Y., Rosenfeld, D. and Li, Z.: A More General Paradigm for Understanding the Decoupling of Stratocumulus-Topped Boundary Layers: The Importance of Horizontal Temperature Advection, Geophys. Res. Lett., doi:10.1029/2020GL087697, 2020.

Zhu, P. and Zuidema, P.: On the use of PDF schemes to parameterize sub-grid clouds, Geophys. Res. Lett., doi:10.1029/2008GL036817, 2009.

Table 1. Dates and time periods of selected non-precipitating MBL cloud periods

Case No.	Start Date	Start UTC	End Date	End UTC	Valid Samples
1	20160915	2200	20160916	0020	24
2	20170219	2110	20170220	0520	87
3	20170222	0830	20170222	1200	38
4	20170605	1430	20170605	1900	54
5	20170616	1230	20170616	1510	32
6	20170617	0320	20170617	0520	24
7	20170627	0020	20170627	0250	28
8	20170630	0530	20170630	0930	42
9	20170630	1400	20170630	1700	34
10	20170706	0140	20170706	0900	62
11	20170707	0130	20170707	1000	91
12	20170910	2100	20170911	0600	94
13	20170911	1930	20170911	2150	24
14	20170912	0820	20170912	1100	32
15	20171006	2110	20171006	2320	26
16	20180130	1030	20180131	0500	152
17	20180203	1930	20180204	0500	72
18	20180324	0210	20180324	0600	46
19	20180508	0730	20180508	1110	42
20	20180513	2130	20180514	1200	139

Table 2. Occurrence frequencies of large in-cloud r_e * under relatively high PWV conditions

| PWV (cm)	1.2-1.4	1.4-1.6	1.6-1.8	2.8-2.0	2.0-2.2	2.2-2.4
$r_e > 12$ μm (%)	25.0	30.6	54.1	74.2	93.8	97.5
$r_e > 14$ μm (%)	1.25	1.77	7.4	17.7	31.9	20.1

*The occurrence of large r_e is defined when the r_e is found to be larger than 12 μm or 14 μm using the retrieved in-cloud vertical profiles.

Table 3. ACI_r calculated with respect to N_{CCN} theoretically at different supersaturation levels, under all PWV_{BL} conditions

PWV_{BL} (cm)	0.4-0.6	0.6-0.8	0.8-1.0	1.0-1.2	1.2-1.4	1.4-1.6	1.6-1.8	1.8-2.0	2.0-2.2	2.2-2.4
ACI_r (N_{CCN}@0.2%SS)	0.020	0.057	0.002	-0.014	0.108	0.076	0.145	0.151	0.221	0.175
(N_{CCN}@0.5%SS)	0.023	0.057	0.0002	0.024	0.129	0.121	0.309	0.136	0.293	0.159
(N_{CCN}@1.2%SS)	0.023	0.045	0.002	0.072	0.125	0.123	0.323	0.175	0.347	0.186

Table 4. The first three principal components from eigenanalysis

Eigenanalysis	PC1	PC2	PC3
Eigenvalues	2.17	1.10	0.91
Proportion of variance explained (%)	43.72	22.01	18.26
Cumulative proportion (%)	43.72	65.73	83.99
Correlations (Variables vs. PCs)	PC1	PC2	PC3
PWV_{BL}	-0.84	0.20	-0.11
D_i	-0.73	-0.48	-0.20
TKE_W	0.69	0.35	-0.44
$W_{dir,ns}$	0.52	0.60	-0.50
LTS	-0.43	0.58	0.65
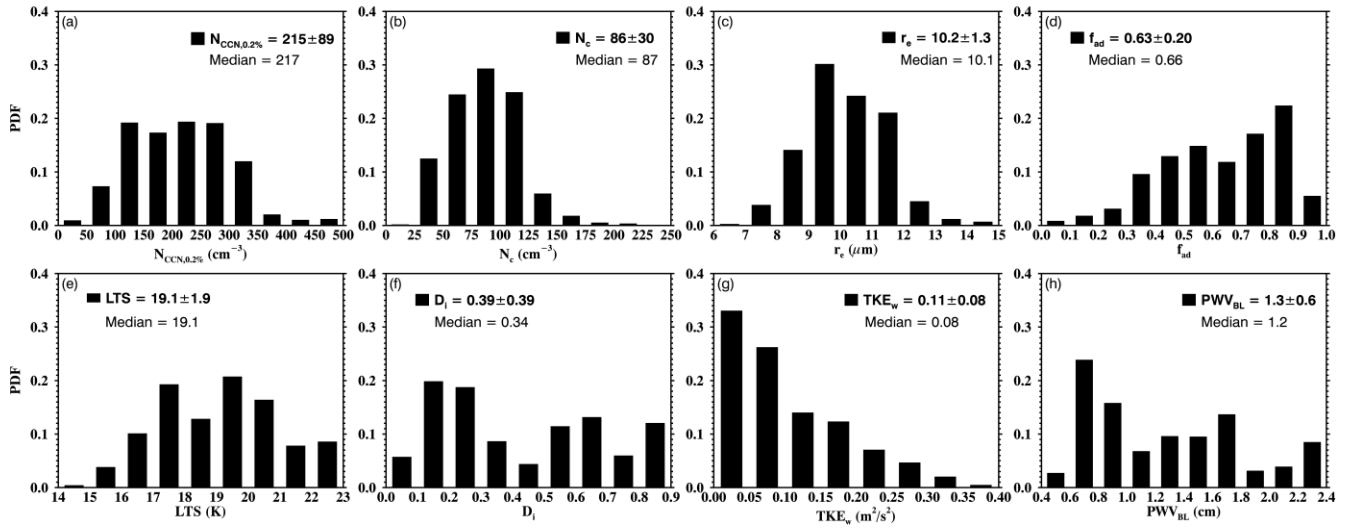
Figure 1. Probability distribution functions (PDFs), mean, standard deviation and median values (dash lines) of aerosol, cloud, and meteorological properties for 20 selected non-precipitating cloud cases at the DOE ENA site during the period 2016-2018. (a) Cloud condensation nuclei (CCN) number concentration at 0.2% supersaturation ($N_{CCN,0.2\%}$); (b) cloud-droplet number concentration (N_c); (c) cloud-droplet effective radius (r_e); (d) cloud adiabaticity (f_{ad}); (e) lower tropospheric stability (LTS); (f) decoupling index (D_i); (g) mean vertical component of turbulence kinetic energy (TKE_w); and (h) sub-cloud boundary-layer precipitable water vapor (PWV_{BL}).
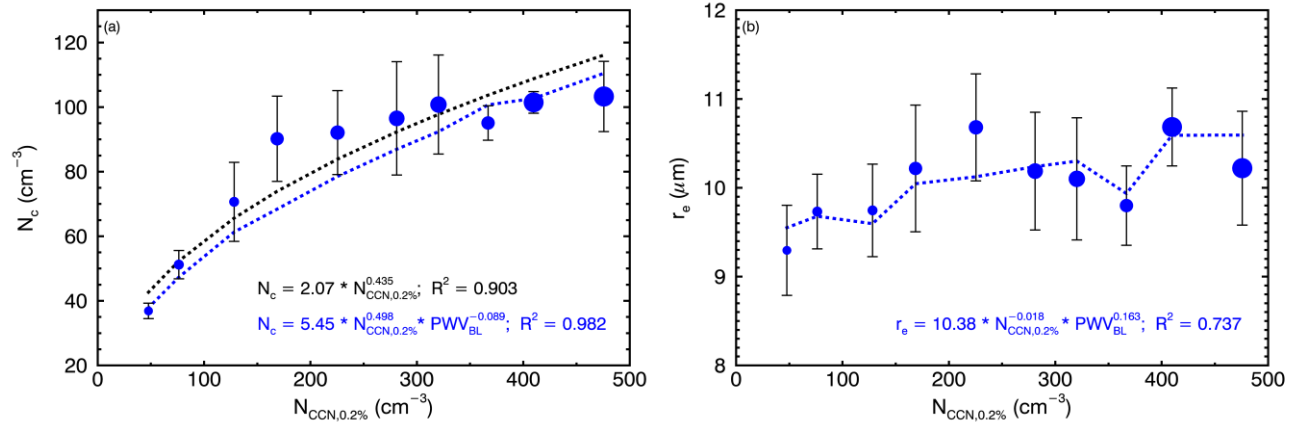
Figure 2. (a) N_c and (b) r_e as a function of $N_{CCN,0.2\%}$ (x-axis) and PWV (blue filled circles) for all selected samples. The larger blue circles represent relatively higher PWV values. Whiskers denote one standard deviation for each bin.
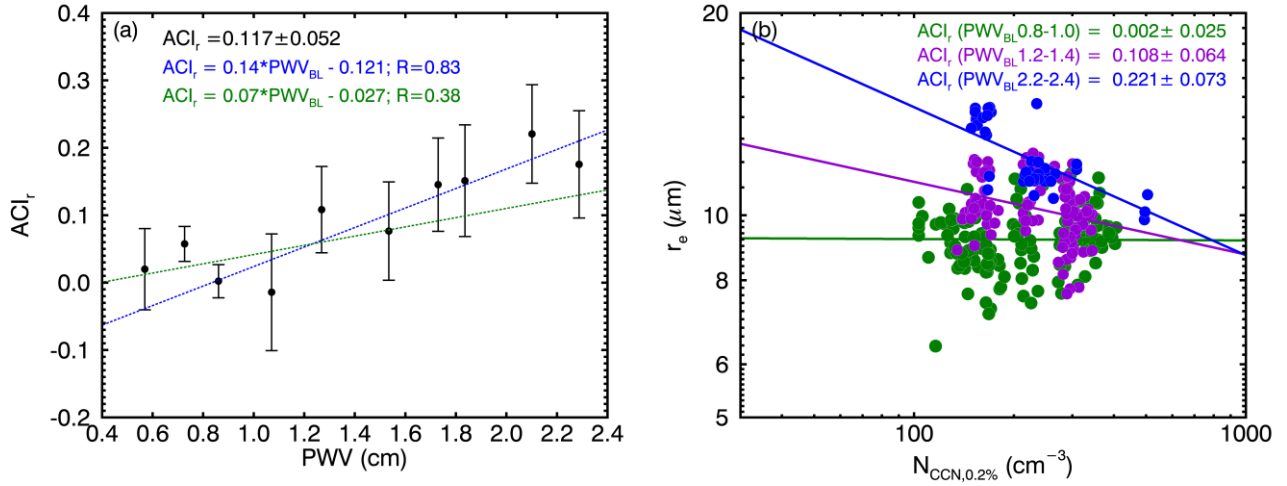
Figure 3. (a) Relationship of ACI_r (dots) to binned PWV_{BL}. Whiskers denote one standard deviation for each bin. Linear regressions are performed in relatively low PWV_{BL} regime (< 1.4 cm, green) and high PWV_{BL} regime (> 1.4 cm); and (b) illustration of ACI_r derived from r_e to $N_{CCN,0.2\%}$ in following three PWV_{BL} bins: 0.8-1.0 cm (green), 1.2-1.4 cm (purple), 2.2-2.4 cm (blue). The ACI_r represents the relative change of r_e with respect to the relative change of $N_{CCN,0.2\%}$, where positive ACI_r denotes the decrease of r_e with increased $N_{CCN,0.2\%}$ under binned PWV.
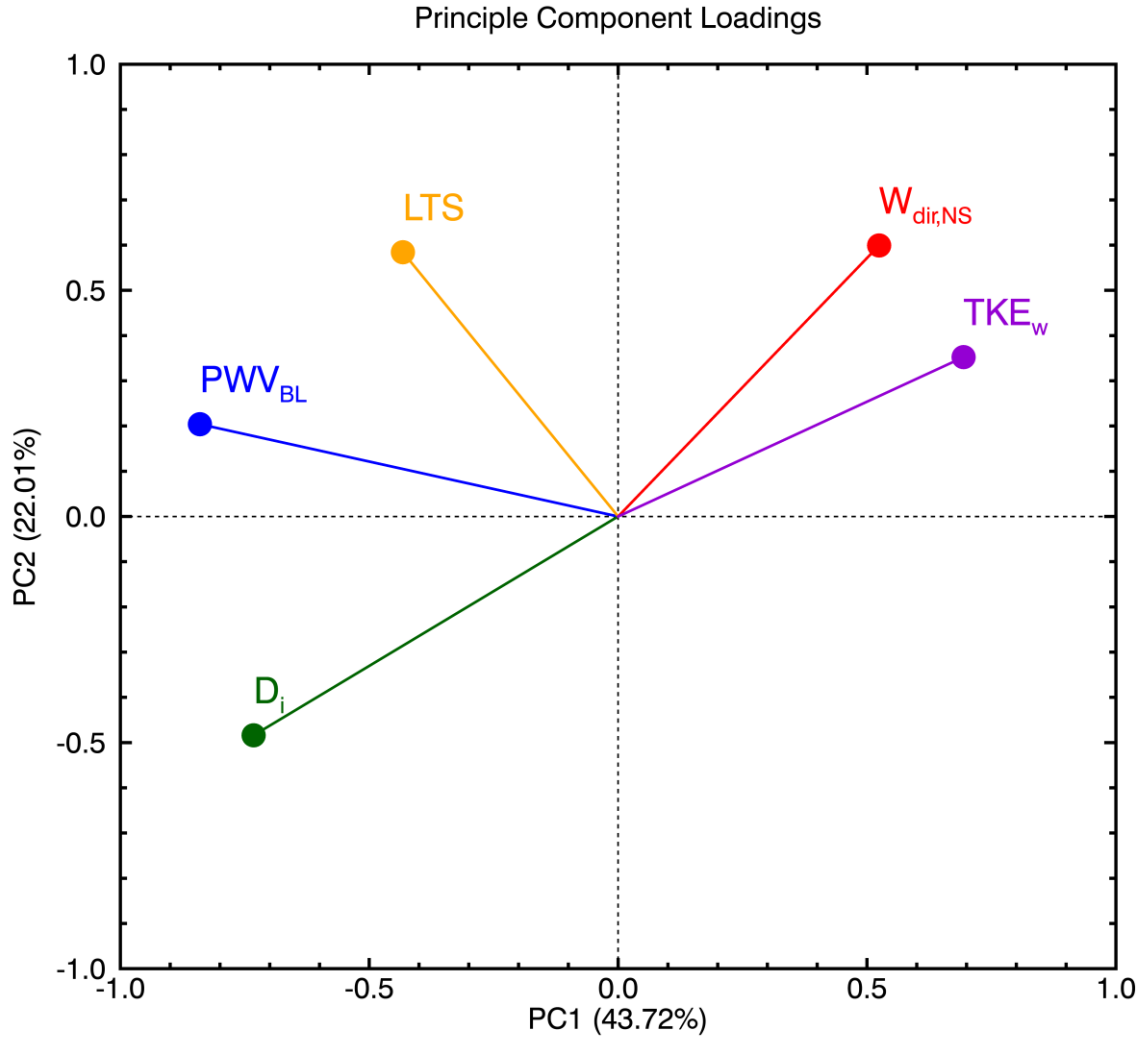
Figure 4. The projections of TKE$_w$ (purple), $W_{dir,NS}$ (red), LTS (orange), PWV$_{BL}$ (blue) and D_i (green) onto the first principal component (PC1) and the second principal component (PC2). The x-coordinates denote variables' correlations with PC1, and the y-coordinates denote variables' correlations with PC2.
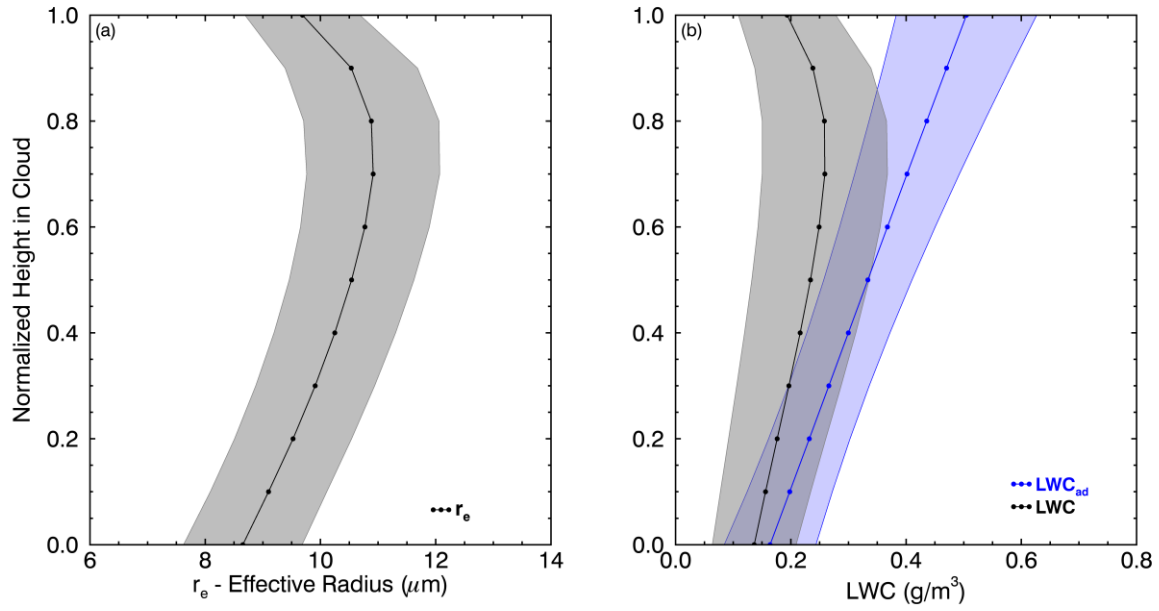
Figure 5. Normalized in-cloud vertical profiles of retrieved (a) r_e and (b) LWC (black) and calculated adiabatic LWC_{ad} (blue) for all selected cloud cases, 0 is cloud base and 1 is cloud top. Solid dotted lines denote mean values and shaded areas denote one standard deviation at each height.
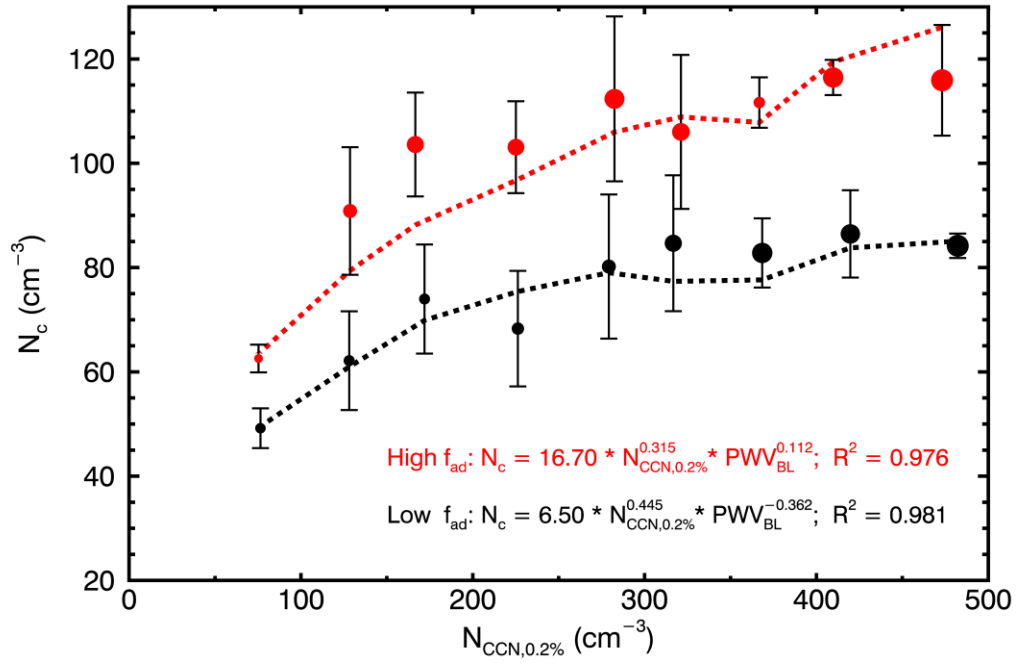
Figure 6. N_c as a function of $N_{CCN,0.2\%}$ (x-axis) and PWV (dots) for high adiabaticity f_{ad} (red) and low f_{ad} (black) regimes. The larger circles represent relatively higher PWV values. Whiskers denote one standard deviation for each bin.
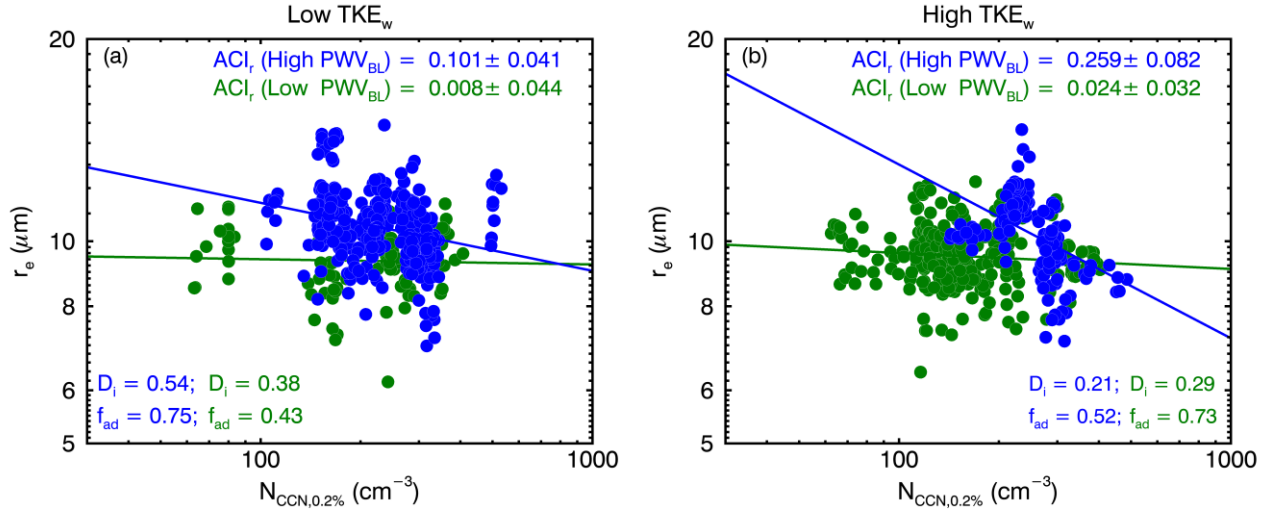
Figure 7. ACI$_r$ derived from r_e to $N_{CCN,0.2\%}$ for (a) low TKE$_w$ and (b) high TKE$_w$ regimes. Samples in the low PWV regime are plotted in green, and samples in the high PWV regime are plotted in blue. The mean values of D_i and f_{ad} are displayed for each quadrant with the corresponding color-coded.
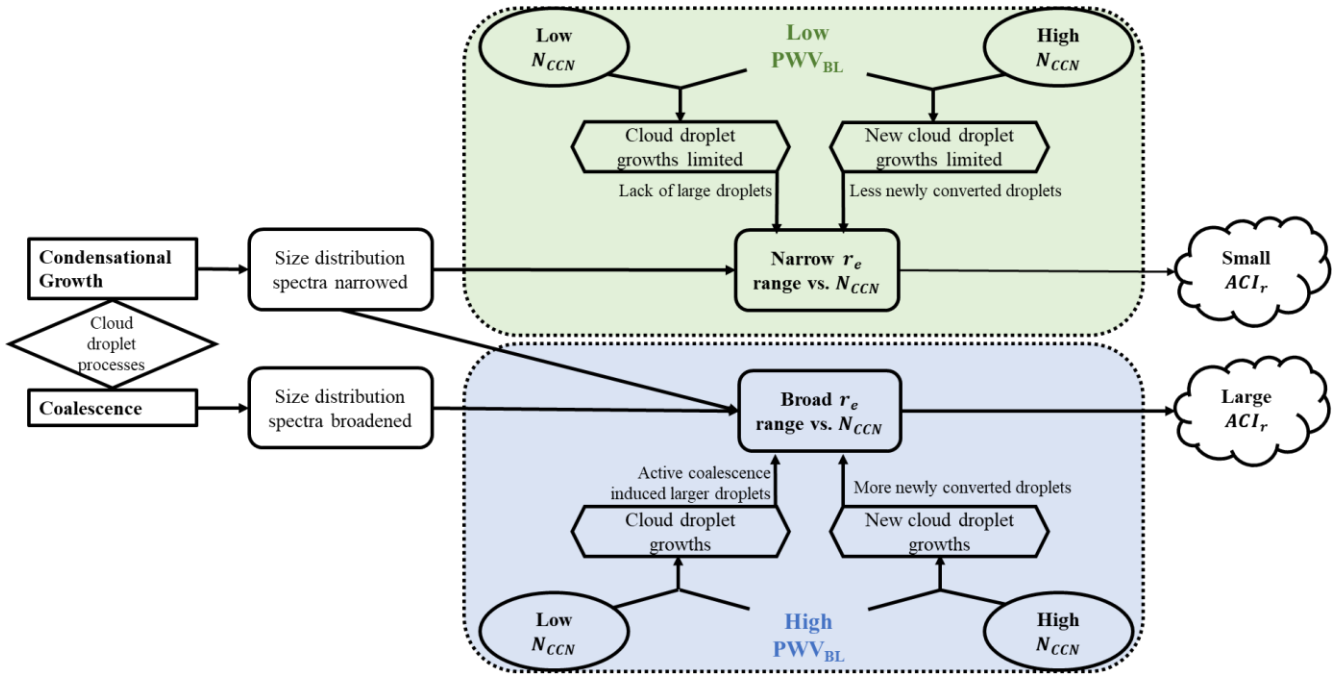
Figure 8. Theoretical mechanism of the responses of cloud droplet size distributions to different CCN intrusion, under relative insufficient (low PWV_{BL}) versus sufficient (high PWV_{BL}) water vapor availabilities.